Chemistry–A European Journal
Research Article
doi.org/10.1002/chem.202401163
Chemistry Europe
European Chemical Societies Publishing
www.chemeurj.org

Monomeric Fe(III)-Hydroxo and Fe(III)-Aqua Complexes Display Oxidative Asynchronous Hydrogen Atom Abstraction Reactivity

Mofijul Molla,[a] Anannya Saha,[b] Suman K. Barman,[b] and Sukanta Mandal*[a]

This paper presents the synthesis and characterization of a series of novel monomeric aqua-ligated iron(III) complexes, $[Fe^{III}(L^{5R})(OH_2)]^{2+}$ (R = OMe, H, Cl, NO_2), supported by an amide-containing pentadentate N_5 donor ligand, L^{5R} [HL^{5R} = 2-(((1-methyl-1*H*-imidazol-2-yl)methyl)(pyridin-2-yl-methyl)amino)-*N*-(5-*R*-quinolin-8-yl)acetamide]. The complexes were characterized by various spectroscopic and analytical techniques, including electrochemistry and magnetic measurements. The Fe(III)-hydroxo complexes, $[Fe^{III}(L^{5R})(OH)]^{1+}$, were generated *in situ* by deprotonating the corresponding aqua complexes in a pH ~7 aqueous medium. In another way, adding one equivalent of a base to a methanolic solution of the Fe(III)-aqua complexes also produced the Fe(III)-hydroxo complexes. The study uses linoleic fatty acid as a substrate to explore the hydrogen atom abstraction (HAA) reactivity of both hydroxo and aqua complexes. The investigation highlights the substitution effect of the L^{5R} ligand on reactivity, revealing a higher rate when an electron-withdrawing group is present. Hammett analyses and(or) determination of the asynchronicity factor (η) suggest an oxidative asynchronous concerted proton-electron transfer (CPET) pathway for the HAA reactions. Aqua complexes exhibited a higher asynchronicity in CPET, resulting in higher reaction rates than their hydroxo analogs. Overall, the work provides insights into the beneficial role of a higher imbalance in electron-transfer-proton-transfer (ET-PT) contributions in HAA reactivity.

Introduction

In recent years, transition-metal-catalyzed C–H bond activation reactions have gained significant attention from researchers. This chemical process holds great importance from both biological and synthetic perspectives, as it represents a critical step in functionalizing C–H substrates to convert them into valuable chemical feedstock.[1–4] The C–H bond oxidation reactions in biological systems generally feature high-valent metal-(hydr)oxo species as common reactive intermediates.[5–12] These intermediates facilitate the oxidation reaction by abstracting a hydrogen atom from the substrate, leading to various transformations such as hydroxylation,[6,12–14] halogenation,[6,15,16] desaturation,[6,11,17] *etc.*

Numerous model studies have been performed on hydrogen atom abstraction (HAA) reactions from X–H substrates (X = C/O) mediated by the high-valent M^{n+}=O intermediates.[6,9,11,12,18–27] However, literature on HAA reactions involving the M^{n+}-OH species, particularly the terminal one, is limited. A few terminal high-valent M(IV)-OH species have been characterized, exhibiting HAA reactions.[28–31] For instance, Busch and co-workers reported a structurally characterized Mn(IV)-bis(hydroxo) complex of a bridged cyclam ligand, which can abstract hydrogen atoms from C–H substrates.[28] Goldberg *et al.* structurally characterized a corrole-based Mn(IV)-OH complex that acts as a powerful hydrogen atom abstractor from phenolic O–H substrates.[29] Cho and co-workers identified a non-heme ligand-supported Mn(IV)-OH species that oxidizes strong aromatic C–H bonds.[30] Paria *et al.* described a high-valent formal Fe(IV)-OH species supported with a redox-non-innocent ligand, which exhibits high reactivity in H-atom abstraction from phenol O–H substrates.[31]

Besides the M(IV)-OH species, the mid-valent terminal M(III)-OH compounds have also been reported as potent oxidants for the C–H and O–H substrates.[32–44] Stack and co-workers prepared terminal Fe(III)–OH[32] and Mn(III)–OH[33] complexes supported by the PY5 ligand {PY5 = 2,6-bis(bis(2-pyridyl)methoxymethane)pyridine}, which are capable of oxidizing C–H substrates through H-atom abstraction. Groves *et al.* reported a hydroxoferric porphyrazine complex that exhibits fast H-atom abstraction from a panel of C–H substrates.[34] The $[(L\text{-}N_4{}^tBu_2)(O_2CPh)Fe^{III}(OH)]^{1+}$ {L-$N_4{}^tBu_2$ = *N,N′*-di-*tert*-butyl-2,11-diaza[3.3](2,6)-pyridinophane} complex[35] of Krüger *et al.* and the $[(dpaq)Mn^{III}(OH)]^{1+}$ {(dpaq = 2-[bis(pyridin-2-ylmethyl)]amino-*N*-quinolin-8-yl-acetamidate)} complex[36] of Jackson *et al.* were remarkable, as these hydroxo complexes abstract hydrogen from various substrates, such as TEMPOH {(TEMPOH = 2,2′-6,6′-tetramethylpiperidine-1-ol)}, phenols, and

[a] M. Molla, S. Mandal
Department of Chemistry, Indian Institute of Technology Kharagpur, Kharagpur, West Bengal 721302, India
E-mail: sukanta.mandal@chem.iitkgp.ac.in
[b] A. Saha, S. K. Barman
Department of Chemical Sciences, Indian Institute of Science Education and Research Mohali, Manauli 140306, India

Supporting information for this article is available on the WWW under https://doi.org/10.1002/chem.202401163

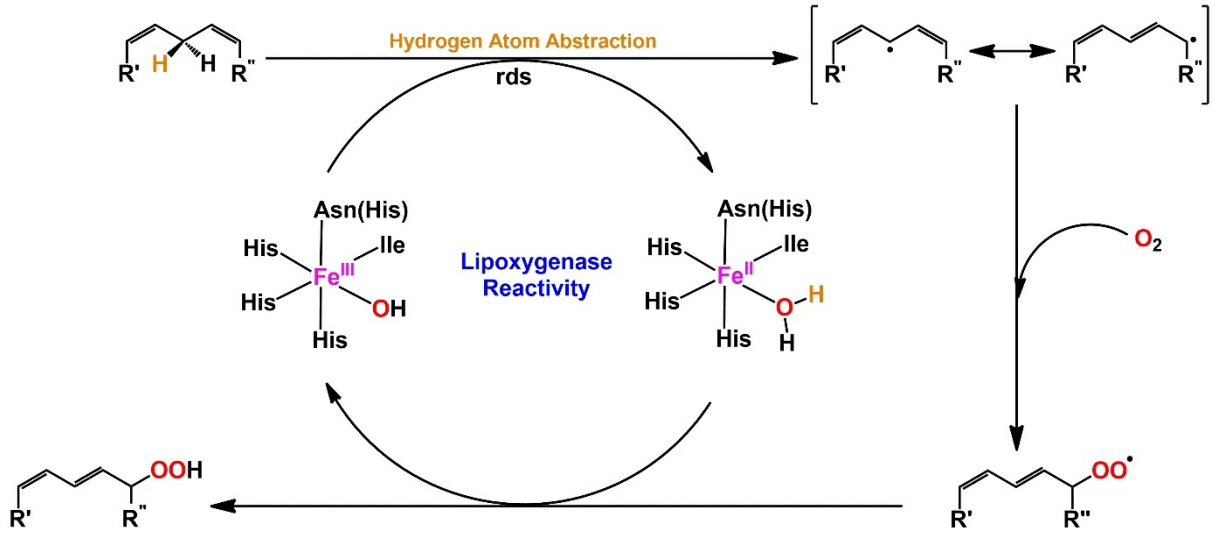

Scheme 1. Generally accepted mechanism of lipoxygenase reactivity.

hydrocarbons. Kovacs's $[Mn^{III}(S^{Me2}N_4(tren))(OH)]^{1+}$ complex displayed the HAA reaction.[37] However, the reactivity with this complex was limited to only the activated O–H bond of TEMPOH. Que *et al.* spectroscopically characterized a transient ferric hydroxo complex, $[Fe^{III}(OH)(TMC\text{-}py)]^{2+}$ {TMC-py = 1-(pyridyl-2'-methyl)-4,8,11-trimethyl-1,4,8,11-tetrazacyclotetradecane}, formed by the reaction of $[Fe^{IV}(O)(TMC\text{-}py)]^{2+}$ with 1,4-cyclohexadiene at −40 °C *via* H-atom abstraction.[38] This $[Fe^{III}(OH)(TMC\text{-}py)]^{2+}$ complex was found capable of oxidizing the O–H bond of TEMPOH. Apart from the iron and manganese complexes, Tolman *et al.* demonstrated C–H/O–H substrate oxidations by Cu(III)-OH complexes.[39,40] A few M(III)-alkoxido complexes (M = Fe, Mn) were also reported, representing the HAA reactions.[41–43]

In recent studies, Fukuzumi, Nam, and co-workers revealed that metal(III)-aqua complexes can also effectively abstract hydrogen atoms, as exemplified with $[(dpaq^{5R})Mn^{III}(OH_2)]^{2+}$ complexes in the oxidation of phenols.[44,45]

The interest in using the terminal metal(III)-hydroxo species as oxidants originates from their crucial involvement in the catalytic event of metalloenzymes such as lipoxygenases (LOs).[46–48] The Fe and Mn LOs employ the Fe(III)-OH and Mn(III)-OH at the active site to oxidize the allylic C–H bond of *cis,cis*-1,4-pentadiene-containing fatty acids. During the enzymatic reaction of Fe-LOs, the active Fe(III)-OH species abstracts a hydrogen atom from the unsaturated fatty acid, producing an allylic radical and the reduced Fe(II)-OH_2 species. The reaction shows a considerable substrate kinetic isotope effect (~50),[49,50] suggesting the rate-limiting cleavage of the C–H bond with a significant tunneling contribution. In the follow-up steps, the resulting allylic radical undergoes an isomerization reaction before it reacts with dioxygen, forming a peroxyl radical. This peroxyl radical further oxidizes Fe(II)-OH_2 back to its active Fe(III)-OH state, completing the catalytic cycle and leading to the dioxygenation of the substrate (Scheme 1). The manganese lipoxygenase is believed to follow a similar pathway.[51,52]

The process of hydrogen-atom abstraction in lipoxygenase-like reactivity is formally equivalent to transferring a proton and an electron from the X–H substrate to the active M(III)-OH center, in which the proton moves to the terminal OH while the electron reduces the M(III) center, forming the M(II)-OH_2 species. Therefore, whether the activation of the X–H bond by the M(III)-OH core is feasible depends on the bond strength of the metal-coordinated water in M(II)(HO–H). For an effective HAA reaction, this O–H bond strength of water in M(II)-OH_2 species should be greater than or comparable to the X–H bond strength in substrates.

The proton-electron transfer (Scheme 2) in the HAA process can occur either in a coupled fashion synchronously (CPET, concerted proton-electron transfer) or in a stepwise manner (PT-ET, proton-transfer/electron-transfer or ET-PT, electron-transfer/proton-transfer). Generally, concerted proton-electron transfer is considered energetically favorable compared to stepwise transfer in the hydrogen-atom transfer mechanism.[53] However, recent reports suggest that H-atom transfer reactions may proceed through asynchronous CPET pathways, where the transition state may contain either a more PT character (referred

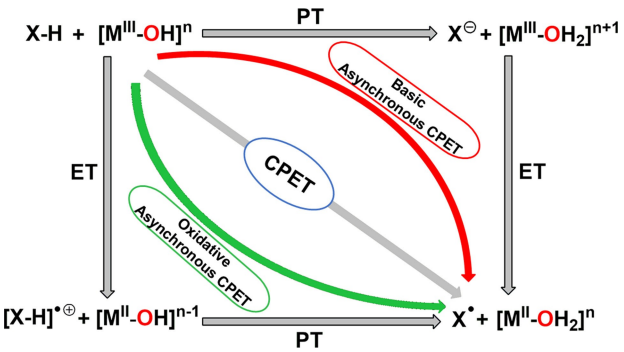

Scheme 2. Concerted *vs* stepwise proton-electron transfer (CPET *vs* PT-ET or ET-PT) for X–H bond activation by a M^{III}-OH species.

to as basic asynchronous CPET) or a more ET character (termed as oxidative asynchronous CPET).[20,27,44,53–56] Exploring the H-atom transfer mechanism and identifying factors influencing the mode of electron-proton transfer remain intriguing subjects, which prompt us to undertake further investigations.

Herein, we report the synthesis and characterization of a set of new monomeric aqua-ligated iron(III) complexes $[Fe^{III}(L^{5R})(OH_2)]^{2+}$ {R = OMe ($\mathbf{1}^{H2O}$), H ($\mathbf{2}^{H2O}$), Cl ($\mathbf{3}^{H2O}$), and NO_2 ($\mathbf{4}^{H2O}$); Figure 1} supported by an amide-containing pentadentate N_5 donor ligand L^{5R} with a substituent at the 5-position {HL^{5R} = 2-(((1-methyl-1*H*-imidazol-2-yl)methyl)(pyridin-2-yl-methyl)amino)-*N*-(5-*R*-quinolin-8-yl)acetamide); R = OMe, H, Cl, NO_2}. In a pH ~7 aqueous medium, each of the Fe^{III}-OH_2 complexes undergoes deprotonation, producing *in situ* the corresponding Fe^{III}-OH complex, $[Fe^{III}(L^{5R})(OH)]^{1+}$ {R = OMe ($\mathbf{1}^{OH}$), H ($\mathbf{2}^{OH}$), Cl ($\mathbf{3}^{OH}$), and NO_2 ($\mathbf{4}^{OH}$)} (Figure 1). Furthermore, adding one equivalent base to each aqua complex's methanol solution also produces the respective hydroxo complex. In the present study, we have examined the hydrogen-atom abstraction reactivity of Fe^{III}-OH ($\mathbf{1}^{OH}$–$\mathbf{4}^{OH}$) and Fe^{III}-OH_2 ($\mathbf{1}^{H2O}$–$\mathbf{4}^{H2O}$) complexes, employing linoleic fatty acid as a substrate. We have observed the substitution effect of the L^{5R} ligand on reactivity for both hydroxo and aqua complexes: a higher reactivity rate is achieved when an electron-withdrawing group is present. Hammett plots and(or) determination of the asynchronicity factor (η) indicate that the HAA reactions proceed *via* an oxidative asynchronous CPET pathway. The Fe^{III}-OH_2 complex displays higher reactivity than its corresponding Fe^{III}-OH complex. This increased reactivity arises from the higher redox potential of the aqua complex relative to its hydroxo counterpart. The higher redox potential contributes to an increased ET character in the transition state, lowering the energy barrier.

Results and Discussion

Synthesis and characterization of Fe(III)-aqua complexes. The ligands HL^{5R} (R = OMe, H, Cl, NO_2) were synthesized following a multistep procedure outlined in Scheme S1. The variation of R substituents at the 5-position of the quinolinyl moiety from electron-donating to electron-withdrawing provides precise control over the electronic characteristics of the ligands. Additionally, these pentadentate ligands leave a coordination site vacant at the metal center, making it accessible for water ligation.

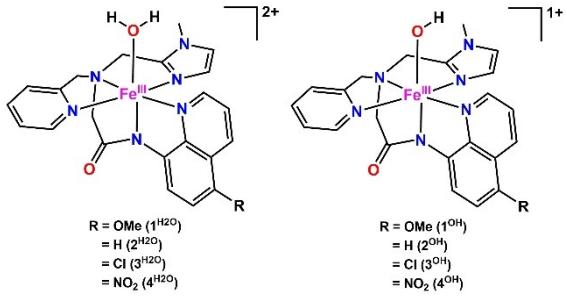

Figure 1. Aqua- and hydroxo-ligated iron(III) complexes.

The ligands were characterized by mass spectrometry (ESI-MS) and spectroscopic techniques such as ATR-FTIR, ^1H and ^{13}C NMR, displayed in Figures S1–S13. Monomeric Fe(III)-aqua complexes, $[Fe^{III}(L^{5R})(OH_2)]^{2+}$ {R = OMe ($\mathbf{1}^{H2O}$), H ($\mathbf{2}^{H2O}$), Cl ($\mathbf{3}^{H2O}$), and NO_2 ($\mathbf{4}^{H2O}$)}, were prepared by reacting the corresponding L^{5R} ligands with $Fe^{III}(ClO_4)_3{\cdot}6H_2O$ in methanol. These aqua complexes were isolated as perchlorate salts and thoroughly characterized using analytical, spectroscopic, and electrochemical techniques, including magnetic susceptibility measurements. In addition, structural characterization for the $\mathbf{3}^{H2O}(ClO_4)_2$ compound was performed by single-crystal X-ray crystallography. The molecular formulas of the complexes were determined through elemental analyses (see the Experimental Section in the Supporting Information).

Mass spectrometry. ESI(+)-MS measurements of compounds $\mathbf{1}^{H2O}(ClO_4)_2$–$\mathbf{4}^{H2O}(ClO_4)_2$ in methanol showed ion peaks associated with formate-bound species at *m/z* 516.1926 $[Fe^{III}(L^{5OMe})(HCOO)]^{1+}$, 486.1700 $[Fe^{III}(L^{5H})(HCOO)]^{1+}$, 520.1327 $[Fe^{III}(L^{5Cl})(HCOO)]^{1+}$, and 531.0950 $[Fe^{III}(L^{5NO2})(HCOO)]^{1+}$, respectively (Figures S14–S17). The source of formate was the ammonium formate buffer used as a mobile-phase additive in the mass spectrometer. These MS data confirm the monomeric nature of these complexes in the solution. Moreover, under experimental mass conditions, the complexes underwent reduction. They transformed to the formal Fe^{II} state, resulting in the emergence of ion peaks at *m/z* values of 471.1911, 441.1693, 475.1325, and 486.1004 corresponding to $[Fe^{II}(L^{5OMe})]^{1+}$, $[Fe^{II}(L^{5H})]^{1+}$, $[Fe^{II}(L^{5Cl})]^{1+}$ and $[Fe^{II}(L^{5NO2})]^{1+}$ species, respectively. The experimental *m/z* values align well with calculated values, and the isotopic distribution patterns closely match the simulated ones.

Infrared spectroscopy. ATR-IR spectra (Figure S18) for the solid samples of compounds $\mathbf{1}^{H2O}(ClO_4)_2{\cdot}2.5H_2O$, $\mathbf{2}^{H2O}(ClO_4)_2$, $\mathbf{3}^{H2O}(ClO_4)_2{\cdot}H_2O$ and $\mathbf{4}^{H2O}(ClO_4)_2{\cdot}H_2O$ displayed strong bands for the carbonyl stretching vibrations of the amide group, $\nu(C{=}O)_{amide}$, between 1592 cm^{-1} and 1657 cm^{-1}.[57,58] The $\nu(C{=}O)_{amide}$ vibrations in complexes $\mathbf{1}^{H2O}$–$\mathbf{4}^{H2O}$ exhibit an increasing trend as the R group of ligands changes from electron-donating to electron-withdrawing: 1592 cm^{-1} ($[Fe(L^{5OMe})(H_2O)]^{2+}$, $\mathbf{1}^{H2O}$) < 1607 cm^{-1} ($[Fe(L^{5H})(H_2O)]^{2+}$, $\mathbf{2}^{H2O}$) < 1626 cm^{-1} ($[Fe(L^{5Cl})(H_2O)]^{2+}$, $\mathbf{3}^{H2O}$) < 1657 cm^{-1} ($[Fe(L^{5NO2})(H_2O)]^{2+}$, $\mathbf{4}^{H2O}$). A good linear correlation between the $\nu(C{=}O)_{amide}$ values and the Hammett constants (σ_{para}) has been observed, as shown in Figure S19. This linear Hammett correlation suggests that R groups at the 5-position of the quinolinyl moiety of ligands influence the amide carbonyl bond strength. The $\nu(ClO_4)$ bands appeared in all complexes at ~1075 cm^{-1} and ~620 cm^{-1}.[59] Complex $\mathbf{4}^{H2O}(ClO_4)_2{\cdot}H_2O$ showed additional bands at 1501 cm^{-1} and 1294 cm^{-1}, corresponding to the nitro group's asymmetric and symmetric stretching vibrations.[58,60] The IR spectra of all four complexes showed broad bands at approximately 3400 cm^{-1}, attributed to the ν(OH) stretching vibrations of water molecules.[61] These bands shifted to a lower wavenumber of about 2400 cm^{-1} in the D_2O-exchanged samples. Notably, no shift in the ν(OH) stretching vibrations was observed when the Fe^{III}-aqua complexes were treated with CD_3OD, implying that

methanol is not a preferred ligand for the Fe(III) center in the present complexes. The IR spectroscopy studies of the deuterated solvent exchange experiments performed with complex $\mathbf{2}^{\mathbf{H2O}}(\mathbf{ClO_4})_2$ are shown in Figure S20. These studies confirm that the O–H vibrations originate from the water molecules present in the complexes.

Magnetic property. Magnetic susceptibilities for powder samples of four Fe^{III}-OH_2 compounds were measured at room temperature (300 K). The effective magnetic moment (μ_{eff}) was calculated to be 5.73μ_B, 5.61μ_B, 5.79μ_B, and 5.74μ_B for the compounds $\mathbf{1}^{\mathbf{H2O}}(\mathbf{ClO_4})_2\cdot\mathbf{2.5H_2O}$, $\mathbf{2}^{\mathbf{H2O}}(\mathbf{ClO_4})_2$, $\mathbf{3}^{\mathbf{H2O}}(\mathbf{ClO_4})_2\cdot\mathbf{H_2O}$ and $\mathbf{4}^{\mathbf{H2O}}(\mathbf{ClO_4})_2\cdot\mathbf{H_2O}$, respectively. These μ_{eff} values indicate that compounds predominantly exist in the high-spin state at room temperature. However, the slightly lower magnetic moments compared to the estimated spin-only value of 5.92μ_B for a purely high-spin ferric complex suggest that the complexes might exhibit thermally induced spin equilibration phenomena. To verify this further, magnetic susceptibility measurements on the powder samples of the compounds were carried out over a temperature range of 300-10 K. Figure S21 demonstrates that the μ_{eff} values of compounds $\mathbf{1}^{\mathbf{H2O}}(\mathbf{ClO_4})_2\cdot\mathbf{2.5H_2O}$, $\mathbf{2}^{\mathbf{H2O}}(\mathbf{ClO_4})_2$, $\mathbf{3}^{\mathbf{H2O}}(\mathbf{ClO_4})_2\cdot\mathbf{H_2O}$, and $\mathbf{4}^{\mathbf{H2O}}(\mathbf{ClO_4})_2\cdot\mathbf{H_2O}$ vary with temperature, decreasing gradually from 5.73μ_B, 5.61μ_B, 5.79μ_B, and 5.74μ_B at 300 K to 1.80μ_B, 2.83μ_B, 2.04μ_B, and 2.03μ_B at 10 K, respectively. These magnetic behaviors unequivocally indicate the presence of a thermal equilibrium between high-spin and low-spin states in all aqua compounds.[62]

Electron paramagnetic resonance (EPR) spectroscopy. The X-band EPR spectra of the Fe(III)-aqua complexes in powder form were recorded at temperatures 300 K and 77 K. The EPR analyses demonstrate the presence of three types of Fe(III) centers within the complex: two types of high-spin (HS) ions (type I: $D < h\nu \sim 0.3\ cm^{-1}$, $E/D = 0$; type II: $D > h\nu \sim 0.3\ cm^{-1}$, $E/D \sim 0.33$) and one of low-spin (LS). For high-spin ions, the position of the EPR signals depends on the relationship between the microwave photon energy ($h\nu$) and the zero-field splitting parameters (D and E). Type I HS Fe^{3+} ions show generally broadened signals at $g \sim 2$, while type II HS Fe^{3+} ions exhibit signals at $g \sim 4.3$.[63–66] The LS Fe^{3+} centers produce sharp isotropic or anisotropic signals with g-tensor values close to 2.[65,66]

At 300 K, the solid-state EPR spectra of the aqua complexes displayed a broad isotropic signal around $g = 2$ (Figure S22). Given that all aqua complexes predominantly exist in the high-spin state at room temperature, as confirmed by the magnetic moment data mentioned earlier, the broad signals at $g \sim 2$ are attributed to type I weakly distorted octahedral Fe(III) complexes ($D < 0.33\ cm^{-1}$, $E = 0$) possessing the $^6A_{1g}$ electronic ground state.[65,66] The spectra of these complexes were simulated using the EasySpin–EPR spectrum simulation program,[67,68] demonstrating smaller D values (0.0041–0.0062 cm^{-1}) with $E/D = 0$ (Table S1). These EPR results are consistent with other reported weakly distorted high-spin Fe(III) complexes.[65,66,69–71]

All complexes experienced a modest spin transition at lower temperatures, as indicated by the EPR spectra (Figure S23), recorded at 77 K in the solid form. At this temperature, each complex's spectrum displayed a distinct anisotropic EPR signal in the high magnetic field region, centered at $g \sim 2$. A very weak signal at $g \sim 4.3$ was also observed in the low-field region, which is attributable to a small fraction of the type II high-spin Fe(III) component with a strong D parameter ($D > h\nu \sim 0.3\ cm^{-1}$) and a low-symmetry ($E/D \sim 0.33$) crystal field environment.[63–66] The high-field region signal of each complex was simulated using the EasySpin[67,68] program. An optimal fitting was achieved by considering a two-component system containing both low-spin ($S = 1/2$)[65,66,71–73] and type I high-spin ($D < 0.33\ cm^{-1}$ and $E/D = 0$)[65,66,69,70] Fe^{3+} ions within the ferric complex (Table S2). Notably, the low-spin components contributed more (~80–87%) to the overall spectral intensity than the high-spin components (~13–20%), consistent with the observed solid-state magnetic behavior of the complexes at lower temperatures.

The Fe(III)-aqua complexes in methanol showed distinct differences in electronic structures compared to solid forms, as revealed by their EPR spectra recorded in methanol. While no EPR signals were detected at room temperature, under frozen conditions at 10 K, all complexes displayed EPR signals in the low-field ($g \sim 8.8$ and 4.3) and high-field regions ($g \sim 2$), as shown in Figure S24. In the low magnetic field region, the sharp isotropic-like signal at $g \sim 4.3$ is attributed to a transition involving the middle Kramers doublet ($M_s = \pm 3/2$), commonly observed for a mononuclear high-spin ferric complex in a highly rhombic environment (type II, $D > h\nu \sim 0.3\ cm^{-1}$, $E/D \sim 0.33$).[63–66,73–75] The weaker signal at $g \sim 8.8$ is tentatively assigned to the ground Kramers doublet ($M_s = \pm 1/2$) transition for an $S = 5/2$ system.[74,75] Conversely, the sharp isotropic (for $\mathbf{2}^{\mathbf{H2O}}$) or anisotropic-type ($\mathbf{1}^{\mathbf{H2O}}$, $\mathbf{3}^{\mathbf{H2O}}$ and $\mathbf{4}^{\mathbf{H2O}}$) signals in the high-field region near $g = 2$ are likely associated with the low-spin ($S = {}^1/_2$) state of the ferric complexes.[41,65,66,71–73] The EPR spectrum of $\mathbf{2}^{\mathbf{H2O}}(\mathbf{ClO_4})_2$ was analyzed further by the EasySpin[67,68] EPR simulation program. The $g = 4.26$ EPR signal was simulated considering an $S = 5/2$ spin-state and rhombic g-tensors ($\mathbf{g}_{\mathbf{real}} = 2.02, 1.99, 1.97$), together with $D = 0.31\ cm^{-1}$ and $E/D = 0.31$. The simulated E/D value of 0.31 authenticates the nearly complete rhombic environment of the Fe^{3+} complex ion in methanol. The $S = 5/2$ rhombogram,[76] shown in Figure S25, illustrates that at an E/D value of ~0.3, the g_x, g_y, and g_z values for the transition between $M_s = \pm 3/2$ doublet converge to an effective $g = 4.3$. This convergence results in an isotropic signal at $g_{eff} = 4.3$, characteristic of a rhombically distorted high-spin Fe(III) complex. The measured g_{eff} value of 4.26 closely aligns with the predicted g_{eff} value of 4.3, fully supporting the assignment of the sharp signal at $g_{eff} = 4.26$ for the transition involving $M_s = \pm 3/2$ doublet, as previously stated. On the other hand, the high-field EPR signal of $\mathbf{2}^{\mathbf{H2O}}(\mathbf{ClO_4})_2$ was successfully modeled considering a low-spin state $S = {}^1/_2$ and $g = 2.124$. A reasonable fit of the overall spectrum was achieved by assigning approximately 90% weightage to the high-spin (type II) and 10% to the low-spin components of the $\mathbf{2}^{\mathbf{H2O}}(\mathbf{ClO_4})_2$ complex (Figure S26). Remarkably, in methanol, complex $\mathbf{2}^{\mathbf{H2O}}$-$(\mathbf{ClO_4})_2$ is predominantly in the high-spin state even at 10 K, in contrast to the phenomenon observed in the solid state. This

observation indicates that the surrounding solvent molecules could influence the electronic structure of Fe^{3+} complex ions.

UV-vis spectroscopy. The UV-vis spectra of complexes $\mathbf{1}^{H2O}(ClO_4)_2$–$\mathbf{4}^{H2O}(ClO_4)_2$ in methanol at room temperature showed strong absorption bands in the 300–400 nm range along with moderately intense broad bands spanning from 550 nm to 950 nm in the visible region (see Experimental Section and Figure S27). The spectra of complexes $\mathbf{1}^{H2O}(ClO_4)_2$–$\mathbf{3}^{H2O}(ClO_4)_2$ featured additional shoulder-type bands within the 425–575 nm range. Magnetic moment calculations have already established that the Fe(III) centers in the present aqua complexes primarily exist in a high-spin state ($S = 5/2$) at room temperature. As such, in an octahedral ligand field environment, *d-d* transitions are spin-forbidden for an $S = 5/2$ spin system. Thus, the observed absorption bands for the Fe(III)-aqua complexes reported here are attributed to charge-transfer transitions. The broad visible absorption bands with $\lambda_{max} = 798$ nm for $\mathbf{1}^{H2O}$, 687 nm for $\mathbf{2}^{H2O}$, 725 nm for $\mathbf{3}^{H2O}$, and 670 nm for $\mathbf{4}^{H2O}$ are tentatively assigned as a ligand to metal charge transfer (LMCT) involving quinoline-amide to Fe(III) charge-transfer.[58] Notably, the LMCT band shifts bathochromically upon substituting the hydrogen atom at the 5-position of the quinoline moiety with the electron-donating methoxy group. In contrast, replacing quinoline 5H with the electron-withdrawing nitro group results in a hypsochromic shift of the LMCT band. Usually, electron-donating groups destabilize the ligand-based orbitals, lowering the energy gap for LMCT transitions, while the reverse is true for electron-withdrawing groups.[73] Nevertheless, the chloro-substitution shows an anomalous trend as the inductive and resonance effects operate reversely.

In pH 4.8 aqueous medium, all complexes exhibited similar spectral characteristics as observed in methanol (see Experimental Section and Figure S28). These observations indicate aqua complexes retain mononuclear structure in the acidic aqueous medium (*vide infra*). However, the band positions are shifted to some extent in water due to the change in the dielectric constant, which may influence the solvation of the excitation transition dipoles.

Structural properties of $[Fe^{III}(L^{5Cl})(OH_2)](ClO_4)_2$ ($\mathbf{3}^{H2O}(ClO_4)_2$). X-ray diffraction-quality single crystals of compound $\mathbf{3}^{H2O}(ClO_4)_2$ were grown by layering *n*-hexane over an acetone solution of the compound. The room temperature XRD analysis reveals that the compound crystallizes in a monoclinic crystal system with the $P2_1$ space group. The asymmetric unit contains two $[Fe^{III}(L^{5Cl})(OH_2)]^{2+}$ complex cations, four ClO_4^- counter anions, and one molecule each of water and acetone as the solvent of crystallization. The two $[Fe^{III}(L^{5Cl})(OH_2)]^{2+}$ cations are designated as cation A and cation B, and they are discriminated by labeling the atoms with suffixes "a" and "b", respectively. The molecular structure of cation A is shown in Figure 2. Table 1 summarizes important bond lengths and angles of cations A and B. Although cations A and B have slight variations in bond lengths and angles, their basic structural features remain consistent. The Fe(III) center is hexa-coordinated in both units, adopting an octahedral geometry with five nitrogen donor atoms from the L^{5Cl} ligand and a water molecule. The donor moieties, namely, the aqua group (O1a/O1b) and the amide nitrogen (N1a/N1b),

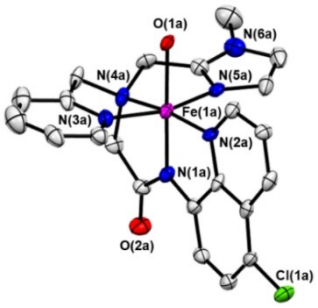

Figure 2. Thermal ellipsoid (40% probability) diagram depicting the molecular structure of cation A in the asymmetric unit of the single-crystal structure of $2\{[Fe^{III}(L^{5Cl})(OH_2)](ClO_4)_2\}\cdot H_2O\cdot(CH_3)_2CO$ (CCDC: 2336880). The diagram does not show perchlorate counter anions and lattice solvent molecules. Carbon atoms are not labeled, and hydrogen atoms are omitted for clarity.

Table 1. Selected bond lengths (Å) and angles (°) of the two $[Fe^{III}(L^{5Cl})(OH_2)]^{2+}$ cations (A and B) in the asymmetric unit.

Fe(1a)–O(1a)	2.021(6)	Fe(1b)–O(1b)	1.997(6)
Fe(1a)–N(1a)	1.841(7)	Fe(1b)–N(1b)	1.846(7)
Fe(1a)–N(2a)	1.968(7)	Fe(1b)–N(2b)	1.954(7)
Fe(1a)–N(3a)	1.969(6)	Fe(1b)–N(3b)	1.955(7)
Fe(1a)–N(4a)	2.012(7)	Fe(1b)–N(4b)	2.004(7)
Fe(1a)–N(5a)	1.936(7)	Fe(1b)–N(5b)	1.945(7)
N(1a)–Fe(1a)–O(1a)	176.1(3)	N(1b)–Fe(1b)–O(1b)	177.0(3)
N(2a)–Fe(1a)–N(4a)	171.3(3)	N(2b)–Fe(1b)–N(4b)	171.4(3)
N(5a)–Fe(1a)–N(3a)	164.6(3)	N(5b)–Fe(1b)–N(3b)	165.9(3)
N(2a)–Fe(1a)–O(1a)	92.9(2)	N(2b)–Fe(1b)–O(1b)	96.1(3)
N(3a)–Fe(1a)–O(1a)	86.2(3)	N(3b)–Fe(1b)–O(1b)	85.4(3)
N(4a)–Fe(1a)–O(1a)	95.8(3)	N(4b)–Fe(1b)–O(1b)	92.4(3)
N(5a)–Fe(1a)–O(1a)	86.1(2)	N(5b)–Fe(1b)–O(1b)	88.0(3)
N(1a)–Fe(1a)–N(2a)	83.5(3)	N(1b)–Fe(1b)–N(2b)	84.0(3)
N(1a)–Fe(1a)–N(3a)	92.8(3)	N(1b)–Fe(1b)–N(3b)	91.5(3)
N(1a)–Fe(1a)–N(4a)	87.8(3)	N(1b)–Fe(1b)–N(4b)	87.5(3)
N(1a)–Fe(1a)–N(5a)	95.8(3)	N(1b)–Fe(1b)–N(5b)	95.0(3)
N(2a)–Fe(1a)–N(3a)	98.0(3)	N(2b)–Fe(1b)–N(3b)	97.9(3)
N(3a)–Fe(1a)–N(4a)	83.1(3)	N(3b)–Fe(1b)–N(4b)	83.7(3)
N(5a)–Fe(1a)–N(2a)	95.7(3)	N(5b)–Fe(1b)–N(2b)	95.1(3)
N(5a)–Fe(1a)–N(4a)	84.4(3)	N(5b)–Fe(1b)–N(4b)	84.2(3)

the pyridyl nitrogen (N3a/N3b) and the imidazole nitrogen (N5a/N5b), and the quinoline nitrogen (N2a/N2b) and the tertiary amine (N4a/N4b) are arranged in a *trans* position to each other in both $[Fe^{III}(L^{5Cl})(OH_2)]^{2+}$ units. For the two structures, the angles between the donor atoms positioned at *cis* and *trans* around the Fe(III) center vary from ~83° to ~98° and ~164° to ~177°, respectively, suggesting that the structure of each cationic unit is somewhat distorted from ideal octahedral geometry. The $Fe–N_{amide}$ bond distance [Fe(1a)-N(1a)/Fe(1b)-N(1b) = 1.841(7) Å/1.846(7) Å] is found to be shorter compared to the other $Fe–N_x$ bond lengths (x = 2a/2b, 3a/3b, 4a/4b, 5a/5b; see Table 1), indicating that the amide nitrogen

forms a strong bond with the Fe(III) center. This robust Fe(III)–N(amide) interaction affects the Fe^{III}–OH_2 bond length in the *trans* position, resulting in an elongated bond distance of Fe(1a/1b)–O(1a/1b) = 2.021(6) Å/1.997(6) Å. The Fe–L bond lengths of the $[Fe^{III}(L^{5Cl})(OH_2)]^{2+}$ complex compare well with those in the crystal structure of the analogous $[Fe^{III}(dpaq)(OH_2)]^{2+}$ complex reported in the literature at 293 K.[57] Surprisingly, the Fe^{III}–N bond distances in the crystal structure of $[Fe^{III}(L^{5Cl})(OH_2)]^{2+}$ at 296 K are shorter than the usual values (Fe–$N_{amine/py}$ = 2.13–2.22 Å) reported for high-spin Fe(III) centers.[73,77,78] Given the observed magnetic moment of ~5.8 μ_B for this complex at room temperature, indicating a predominance of the high-spin state, we believe that the molecular structure of the $[Fe^{III}(L^{5Cl})(OH_2)]^{2+}$ complex may represent an exceptional case for a high-spin structure. However, the reason behind this unusual observation remains unclear to us. The substituents R at the 5-position of the quinolinyl group in the ligand can control the donor property of the amide nitrogen, which in turn can potentially influence the structural and electronic properties of the $[Fe^{III}(L^{5R})(OH_2)]^{2+}$ complexes. A comparative structural analysis of the $[Fe^{III}(L^{5R})(OH_2)]^{2+}$ derivatives would have been enlightening. However, such studies could not be completed because of the unavailability of the crystal structure of other $[Fe^{III}(L^{5R})(OH_2)](ClO_4)_2$ (R = OMe, H, NO_2) complexes.

Electrochemical study. The redox properties of complexes $\mathbf{1^{H2O}(ClO_4)_2}$–$\mathbf{4^{H2O}(ClO_4)_2}$ were investigated by cyclic voltammogram in a methanol solvent, depicted in Figure S29. Each of the Fe(III)-aqua complexes displayed a quasi-reversible Fe^{III}/Fe^{II} redox event at the potential, $E_{1/2}$ = 0.322 V for $\mathbf{1^{H2O}}$, 0.348 V for $\mathbf{2^{H2O}}$, 0.396 V for $\mathbf{3^{H2O}}$, and 0.494 V for $\mathbf{4^{H2O}}$, referenced *versus* NHE. The $E_{1/2}$ values linearly correlate with the Hammett constants (σ_p) of the substituents, shown in Figure S30. This correlation indicates that the R group at the 5-position of the quinolinyl moiety in the L^{5R} ligands affects the reduction potential of the Fe(III) center in $[Fe^{III}(L^{5R})(OH_2)]^{2+}$ complexes.

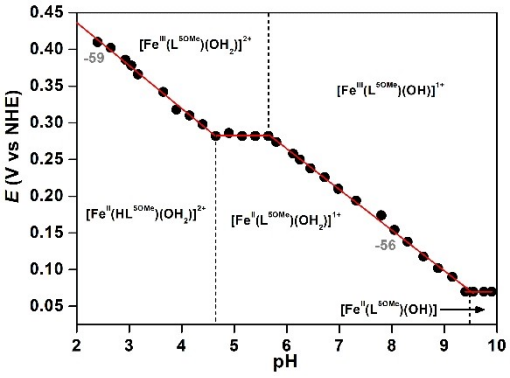

Figure 3. Pourbaix diagram of complex $[Fe^{III}(L^{5OMe})(OH_2)]^{2+}$ ($\mathbf{1^{H2O}}$) over a pH range from 2 to 10.

To explore the proton-coupled-electron-transfer (PCET) redox processes associated with these Fe(III)-OH_2 complexes, electrochemical studies were conducted in an aqueous medium over a pH range from 2 to 10. Figure 3 shows the Pourbaix diagram of complex $\mathbf{1^{H2O}}$. The diagrams for $\mathbf{2^{H2O}}$–$\mathbf{4^{H2O}}$ are depicted in Figure S31. Figure S32 displays a few representative CV and DPV diagrams for complex $\mathbf{1^{H2O}}$ at various pH levels.

Each complex's Pourbaix diagram displays pH-dependent and -independent Fe^{III}/Fe^{II} reduction potentials. The pH-independent redox behavior is indicative of the transfer of electrons only, attributable to the $[Fe^{III}(L^{5R})(OH_2)]^{2+}/[Fe^{II}(L^{5R})(OH_2)]^{1+}$ and $[Fe^{III}(L^{5R})(OH)]^{1+}/[Fe^{II}(L^{5R})(OH)]$ redox couples depicted in the diagrams. Conversely, the pH-dependent Fe^{III}/Fe^{II} reduction potential, with a slope of approximately 59 mV/pH, indicates a one-electron and one-proton PCET process ascribed to the $[Fe^{III}(L^{5R})(OH_2)]^{2+}/[Fe^{II}(HL^{5R})(OH_2)]^{2+}$ and $[Fe^{III}(L^{5R})(OH)]^{1+}/[Fe^{II}(L^{5R})(OH_2)]^{1+}$ redox couples in the diagrams. The redox potentials of the $[Fe^{III}(L^{5R})(OH_2)]^{2+}/[Fe^{II}(L^{5R})(OH_2)]^{1+}$ and $[Fe^{III}(L^{5R})(OH)]^{1+}/[Fe^{II}(L^{5R})(OH)]$ couples along with the pK_a values of $[Fe^{II}(\mathbf{H}L^{5R})(OH_2)]^{2+}$, $[Fe^{III}(L^{5R})(O\mathbf{H}_2)]^{2+}$ and $[Fe^{II}(L^{5R})(O\mathbf{H}_2)]^{1+}$ species in water have been determined from the Pourbaix diagrams and the data are summarized in Table 2. Notably, the acidity of coordinated water decreases by approximately four orders of magnitude when reduced from $[Fe^{III}(L^{5R})(OH_2)]^{2+}$ to $[Fe^{II}(L^{5R})(OH_2)]^{1+}$. This phenomenon concurs well with what one would expect from the metal ion Lewis acidity at higher and lower oxidation states. As can be found in Table 2, the redox potential and the pK_a values follow a substituent-dependent order: the potential increases, whereas the pK_a decreases as the electron-withdrawing character of the substituent gradually increases.

Formation of hydroxo-ligated $[Fe^{III}(L^{5R})(OH)]^{1+}$ complexes ($\mathbf{1^{OH}}$–$\mathbf{4^{OH}}$) and their properties. The addition of 1,8-diazabicyclo[5.4.0]undec-7-ene (DBU) to a methanol solution of the $[Fe^{III}(L^{5R})(OH_2)]^{2+}$ ($\mathbf{1^{H2O}}$–$\mathbf{4^{H2O}}$) complexes afforded the formation of ferric hydroxo complexes $[Fe^{III}(L^{5R})(OH)]^{1+}$ ($\mathbf{1^{OH}}$–$\mathbf{4^{OH}}$). Figure S33 presents the UV-vis spectral changes during the conversion from "Fe^{III}–OH_2" to "Fe^{III}–OH" in methanol. The broad absorption bands of the aqua complexes in the visible range (600–1000 nm) gradually diminished with the progressive addition of DBU, showing isosbestic points. Titration experiments demonstrated that one equivalent of DBU is needed to

Table 2. Redox potentials and pK_as of iron complexes in an aqueous medium determined from the Pourbaix diagrams.

R	E (V vs NHE) $[Fe^{III}(L^{5R})(OH_2)]^{2+}/[Fe^{II}(L^{5R})(OH_2)]^{1+}$	E (V vs NHE) $[Fe^{III}(L^{5R})(OH)]^{1+}/[Fe^{II}(L^{5R})(OH)]$	pK_a $[Fe^{II}(\mathbf{H}L^{5R})(OH_2)]^{2+}$	pK_a $[Fe^{III}(L^{5R})(O\mathbf{H}_2)]^{2+}$	pK_a $[Fe^{II}(L^{5R})(O\mathbf{H}_2)]^{1+}$
OMe	0.283	0.070	4.64	5.65	9.47
H	0.303	0.101	4.52	5.48	9.30
Cl	0.342	0.138	4.27	5.40	9.19
NO_2	0.373	0.182	4.03	5.34	8.98

fully form the Fe(III)–OH complexes (Figure S33, inset). Mass spectrometry analysis was conducted to identify the $[Fe^{III}(L^{5R})(OH)]^{1+}$ species in methanol. Triethylamine was used as a base instead of DBU to generate the hydroxo species for mass analysis to avoid potential damage to the mass spectrometer by DBU. Figures S34–S37 display the ESI(+) mass spectra of complexes $\mathbf{1^{H2O}(ClO_4)_2}$–$\mathbf{4^{H2O}(ClO_4)_2}$ dissolved in methanol containing one equivalent of triethylamine. Intense signals were observed at *m/z* 488.1304, 458.1178, 492.0807, and 503.1039 corresponding to the monomeric $[\mathbf{1^{OH}}]^{1+}$, $[\mathbf{2^{OH}}]^{1+}$, $[\mathbf{3^{OH}}]^{1+}$ and $[\mathbf{4^{OH}}]^{1+}$ species, respectively. In addition to the hydroxo species signals, the mass spectra of the iron compounds in the basic medium showed prominent peaks at *m/z* about one mass unit less than those of $[Fe^{III}(L^{5R})(OH)]^{1+}$ *viz* 487.1241, 457.1111, 491.0741, and 502.0976, which are attributed to the monocationic formal Fe(IV)-oxido species $[Fe^{IV}(L^{5OMe})(O)]^{1+}$, $[Fe^{IV}(L^{5H})(O)]^{1+}$, $[Fe^{IV}(L^{5Cl})(O)]^{1+}$, and $[Fe^{IV}(L^{5NO2})(O)]^{1+}$, respectively. Since these mass spectrometry experiments were conducted using analytically and spectroscopically pure Fe(III)-aqua complexes, probably, the $[Fe^{IV}(L^{5R})(O)]^{1+}$ species were generated from the $[Fe^{III}(L^{5R})(OH)]^{1+}$ complexes *via* one-electron-one-proton PCET oxidation under the experimental mass conditions. Notably, no signals corresponding to Fe^{III}-OMe complexes or μ-oxo bridged dimeric complexes were detected, thus excluding their formation in a methanolic medium. The EPR spectra (Figure S38) of all four hydroxo compounds under frozen conditions in methanol at 10 K exhibited an intense signal at $g_{eff} = 4.26$, representing a rhombically distorted high-spin Fe(III) state, as discussed previously.[63–66,73–75]

The ferric hydroxo complexes could also be generated in water by adjusting the pH appropriately. The Pourbaix diagram of $[Fe^{III}(L^{5R})(OH_2)]^{2+}$ ($\mathbf{1^{H2O}}$–$\mathbf{4^{H2O}}$) complexes estimated the stability region of the hydroxo-ligated $[Fe^{III}(L^{5R})(OH)]^{1+}$ ($\mathbf{1^{OH}}$–$\mathbf{4^{OH}}$) species within the pH range of ~5.5 to 10. The conversions from "Fe^{III}–OH_2" to "Fe^{III}–OH" species were monitored by UV-vis spectroscopy as a function of pH in an aqueous medium. The aqua complexes' visible-region (600–1000 nm) characteristic broad absorption band disappeared as the pH increased gradually from 4 to 7.5. These spectral changes, depicted in Figure 4, exhibit isosbestic points, indicating a clean transformation from the "Fe^{III}–OH_2" complex to the "Fe^{III}–OH" species in water. Interestingly, the transformations between "Fe^{III}–OH_2" and "Fe^{III}–OH" are reversible. As demonstrated in Figure S39, the aqua complexes could be regenerated from the hydroxo complexes by adjusting the pH from neutral to acidic conditions. The mass-spectrometry analysis confirmed the formation of hydroxo species in neutral pH. ESI(+)-MS measurement of $\mathbf{1^{H2O}(ClO_4)_2}$–$\mathbf{4^{H2O}(ClO_4)_2}$ complexes in a pH 7 aqueous medium showed prominent peaks at *m/z* 488.1222 $[\mathbf{1^{OH}}]^{1+}$, 458.1116 $[\mathbf{2^{OH}}]^{1+}$, 492.0730 $[\mathbf{3^{OH}}]^{1+}$, and 503.0986 $[\mathbf{4^{OH}}]^{1+}$, respectively, affirming the formation of monomeric $[Fe^{III}(L^{5R})(OH)]^{1+}$ species in the solution (Figures S40–S43). Nevertheless, the ESI(+)-MS data for the Fe^{III}-hydroxo complexes in pH 7 aqueous medium contain many peaks, including the peak attributed to $[Fe^{IV}(L^{5R})(O)]^{1+}$ species, which could suggest a complex speciation. Thus, to quantify the amount of Fe^{III}-hydroxo species produced from the Fe^{III}-aqua complexes under neutral pH conditions, we performed EPR spin concentration measurement of the high-spin $S = 5/2$ rhombic Fe(III) signals (g_{eff} ~ 4.3) of the Fe^{III}-hydroxo species, considering the g_{eff} ~ 4.3 signal of the high-spin Na[Fe^{III}(EDTA)] (H_4EDTA = ethylenediaminetetraacetic acid) complex as a standard.[79] Figure S44 depicts the EPR spectrum of a frozen solution of $\mathbf{3^{H2O}}$ (1 mM) in pH 7.15 at 10 K, alongside the spectrum of the standard Fe^{3+}-EDTA under the same conditions. The absolute area of the g ~ 4.26 signal for Fe(III) of $\mathbf{3^{OH}}$ closely matched that of the area obtained for the Fe^{3+}-EDTA, attesting to the quantitative formation of the Fe^{III}-hydroxo species at neutral pH conditions. Similar EPR spin quantification studies conducted with other Fe(III)-aqua complexes at pH 7.15 confirmed the complete formation of respective Fe(III)-hydroxo complexes.

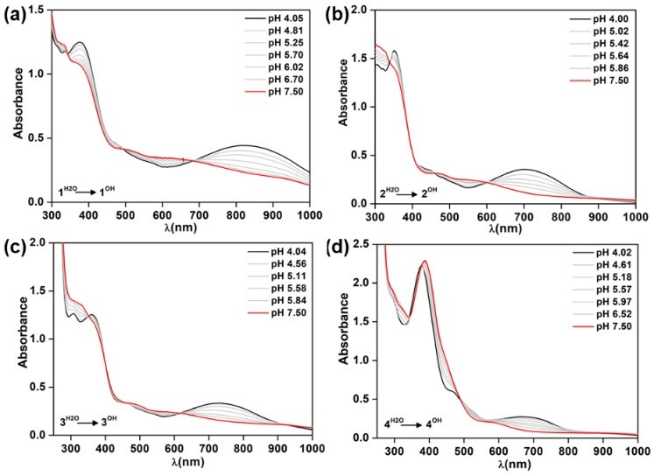

Figure 4. UV-vis spectral changes for the conversion of "Fe^{III}-OH_2" to "Fe^{III}-OH", varying pH from 4 to 7.5: (a) $\mathbf{1^{H2O}} \rightarrow \mathbf{1^{OH}}$; (b) $\mathbf{2^{H2O}} \rightarrow \mathbf{2^{OH}}$; (c) $\mathbf{3^{H2O}} \rightarrow \mathbf{3^{OH}}$; (d) $\mathbf{4^{H2O}} \rightarrow \mathbf{4^{OH}}$.

Monomeric Fe(III)-hydroxo complexes are rare as they usually form oxo-bridged dimers. These dimers are generally EPR silent at low temperatures due to strong antiferromagnetic exchange coupling between two Fe(III) centers.[80–82] Although we did not isolate the hydroxo complexes ($\mathbf{1^{OH}}$–$\mathbf{4^{OH}}$), their EPR active status supports their existence in monomeric forms, particularly in protic solvents like MeOH or H_2O. In methanol or water, solvent molecules participating in hydrogen-bonding interactions likely surround the hydroxo of Fe(III)–OH, preventing the Fe(III)–OH unit from forming dimers. Alternatively, the hydroxo group of $[Fe^{III}(L^{5R})(OH)]^{1+}$ might engage in a hydrogen-bonding interaction with the amide oxygen of another $[Fe^{III}(L^{5R})(OH)]^{1+}$ molecule. This intermolecular H-bonding interaction could stabilize the monomeric Fe(III)–OH structure, as found in the crystal structure of the $[Mn^{III}(dpaq)(OH)]^{1+}$ complex reported by Jackson *et al.*[36]

Computed structures of the Fe^{III}-hydroxo complexes. Density functional theory (DFT) calculations were employed to elucidate the structural features of the *in situ* generated Fe(III)-hydroxo complexes, considering a methanol solvation model. We focus on high-spin states ($S = 5/2$) since the Fe(III)-hydroxo complexes primarily adopt high-spin structures in methanol as

determined by EPR studies (*vide supra*). Figure 5 displays the DFT-optimized structure of the $[Fe^{III}(L^{5Cl})(OH)]^{1+}$ complex ion in the sextet state, while the remaining structures can be found in Figure S45 of the Supporting Information. The computed structures of $[Fe^{III}(L^{5R})(OH)]^{1+}$ complexes reveal a distorted octahedral geometry of the Fe(III) centers, featuring short Fe(III)–O(H) distances of 1.878 Å for $\mathbf{1}^{OH}$, 1.876 Å for $\mathbf{2}^{OH}$, 1.873 Å for $\mathbf{3}^{OH}$, and 1.866 Å for $\mathbf{4}^{OH}$. These calculated distances closely align with those reported for other high-spin octahedral Fe(III)-OH complexes with known structures.[35,83,84] Although the differences in the Fe(III)–O(H) distances among the hydroxo complexes in this series are quite small, we observed a trend of decreasing Fe(III)–O(H) bond distances with increasing electron-withdrawing ability of the 5-R substituents. This observation is consistent with a previously reported computational prediction in the literature, which noted a similar trend in the variation of Mn(III)–O(H) bond lengths for $[Mn^{III}(dpaq^{5R})(OH)]^{1+}$ complexes (R = OMe, H, Cl, NO_2).[85]

Furthermore, structures for $\mathbf{3}^{OH}$ in the low-spin ($S = {}^1/_2$) and intermediate-spin ($S = 3/2$) states were calculated as representatives to examine any structural variances across different spin states. Table S3 presents DFT-predicted Fe^{III}–L distances for $\mathbf{3}^{OH}$ in different spin states. Notably, the low-spin state exhibits shorter bond lengths and less distortion, while the high-spin state shows longer bond distances and more distortion.

Determination of bond strength of metal coordinated water in the reduced $[Fe^{II}(L^{5R})(OH_2)]^{1+}$ species. The capacity of

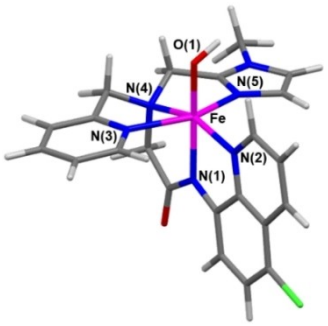

Figure 5. DFT-optimized structure of $[Fe^{III}(L^{5Cl})(OH)]^{1+}$ ($\mathbf{3}^{OH}$) complex ion in the sextet state. Selected bond lengths: Fe–O(1) = 1.873 Å, Fe–N(1) = 2.091 Å, Fe–N(2) = 2.144 Å, Fe–N(3) = 2.211 Å, Fe–N(4) = 2.288 Å, Fe–N(5) = 2.156 Å. Color code: Fe, magenta; C, gray; N, blue; O, red; Cl, green; H, white.

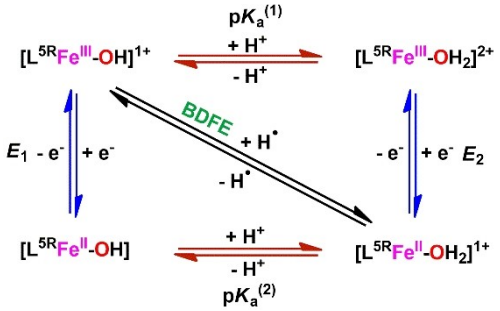

Scheme 3. Thermodynamic square scheme for calculating the BDFE of the O–H bond in the coordinated water of $[L^{5R}Fe^{II}\text{-}OH_2]^{1+}$.

Fe(III)-hydroxo complexes, $[Fe^{III}(L^{5R})(OH)]^{1+}$, abstracting a hydrogen atom from X–H substrates, depends on the strength of the O–H bond being formed in $[Fe^{II}(L^{5R})(HO\text{–}H)]^{1+}$ product and the X–H bond being broken. From a thermodynamic perspective, the Fe^{II}-(HO–H) bond strength should be greater than or equivalent to the bond strength of the X–H substrates for an effective hydrogen atom abstraction reaction. The bond dissociation free energy (BDFE) of the O–H bond in the coordinated water of $[Fe^{II}(L^{5R})(OH_2)]^{1+}$ complexes can be calculated using the square diagram shown in Scheme 3 and the Bordwell[86,87] equation: $BDFE(Fe^{II})(HO\text{–}H) = 23.06E_{1/2}(Fe^{3+}/Fe^{2+}) + 1.37(pK_a) + C_{G,sol}$, where the constant $C_{G,sol}$ represents the formation and solvation energies of $H^\bullet$ in a specific solvent ($C_{G,H2O} = 52.8$ kcal/mol).[87] In Scheme 3, the diagonal line represents the concerted proton-electron transfer (CPET), which can be decomposed into the stepwise transfer of electrons (vertical lines) and protons (horizontal lines).

For our system, we experimentally determined the redox potential of the $[Fe^{III}(L^{5R})(OH_2)]^{2+}/[Fe^{II}(L^{5R})(OH_2)]^{1+}$ and $[Fe^{III}(L^{5R})(OH)]^{1+}/[Fe^{II}(L^{5R})(OH)]$ couples, as well as the pK_a value of the $[Fe^{III}(L^{5R})(OH_2)]^{2+}$ and $[Fe^{II}(L^{5R})(OH_2)]^{1+}$ species in an aqueous medium from the Pourbaix diagrams (see Table 2). So, the BDFEs can be calculated by considering both thermodynamic cycles (two triangles in Scheme 3), which account for (i) the one-electron reduction of Fe^{III}–OH_2 to Fe^{II}–OH_2 and the deprotonation of Fe^{III}–OH_2 to produce Fe^{III}–OH, and (ii) the one-electron reduction of Fe^{III}–OH to Fe^{II}–OH and the deprotonation of Fe^{II}–OH_2 to form Fe^{II}–OH. Using both approaches, the average BDFEs(O–H) for $[Fe^{II}(L^{5OMe})(HO\text{–}H)]^{1+}$, $[Fe^{II}(L^{5H})(HO\text{–}H)]^{1+}$, $[Fe^{II}(L^{5Cl})(HO\text{–}H)]^{1+}$, and $[Fe^{II}(L^{5NO2})(HO\text{–}H)]^{1+}$ in a water solvent are determined to be 67.23 ± 0.15 kcal/mol, 67.59 ± 0.28 kcal/mol, 68.33 ± 0.24 kcal/mol, and 69.01 ± 0.29 kcal/mol, respectively. These O–H BDFE values of the present systems are higher than that of the Kovacs's $[Fe^{II}(^{OMe2}N_4(tren))(OH_2)]^{1+}$ complex[88] determined in a water medium (63.8 kcal/mol; modified value considering $C_{G,H2O} = 52.8$ kcal/mol).[87]

Two crucial factors, Fe^{3+}/Fe^{2+} redox potential and pK_a, regulate the strength of the O–H bond in the Fe^{II}-(HO–H) product. However, these factors exhibit a reverse relationship, where an increase in Fe^{3+}/Fe^{2+} redox potential leads to a simultaneous decrease in the pK_a of coordinated water and *vice versa*. Figure S46 illustrates the contributions from the $E_{1/2}$ and pK_a values to the overall BDFE as a function of the Hammett constant (σ_{para}) of the 5-substituent of the L^{5R} ligand. The slopes of the lines in Figure S46 indicate that variations in $E_{1/2}$ have a more pronounced effect on the BDFE as a function of σ_{para} compared to pK_a variations, resulting in an overall increase in BDFE values for more electron-withdrawing groups. However, the net difference in Fe^{II}–H(O–H) BDFE between the lowest $[Fe^{II}(L^{5OMe})(OH_2)]^{1+}$ and the highest $[Fe^{II}(L^{5NO2})(OH_2)]^{1+}$ in this series is only 1.78 kcal/mol. This slight difference in BDFE values is due to the contrasting effect of changes in $E_{1/2}$ and pK_a.

Kinetic studies of peroxidation of linoleic acid catalyzed by the Fe^{III}-hydroxo complexes. The study utilized natural linoleic fatty acid as a model substrate to explore the lipoxygenase-like reactivity of Fe^{III}-hydroxo ($\mathbf{1}^{OH}$–$\mathbf{4}^{OH}$) complexes. The calculated BDFE value for the C(11)–H bond in linoleic acid

was found to be 65.98 ± 0.06 kcal/mol, which is lower than the Fe^{II}–H(O–H) BDFE values in the present series of complexes (*vide supra*). So, the hydrogen atom abstraction from the C(11)–H bond by the $[Fe^{III}(L^{5R})(OH)]^{1+}$ (R = OMe, H, Cl, NO_2) complexes is thermodynamically feasible. The reactions were carried out in a pH 7.15 aqueous buffer-methanol mixture, which ensured nearly quantitative generation of the hydroxo species from the corresponding aqua complex. Kinetic experiments were performed under pseudo-first-order conditions by adding an excess of substrate (20–80 equivalents) to the $[Fe^{III}(L^{5R})(OH)]^{1+}$ complexes at room temperature in the presence of dioxygen. The peroxidation of the linoleic acid was assessed by adding thiobarbituric acid (TBA), which produced pink colorations with absorbance bands at 455 nm and 532 nm.[42,89,90] In the proposed mechanism, illustrated in Scheme 1, the $[Fe^{III}(L^{5R})(OH)]^{1+}$ complexes abstract a hydrogen atom from the C(11)–H bond of linoleic acid, producing a radical that reacts with dioxygen to form a peroxyl radical. This peroxyl radical then oxidizes the $[Fe^{II}(L^{5R})(OH_2)]^{1+}$ complexes, transforming into the hydroperoxide species. The hydroperoxide undergoes oxidative cleavage into alkanals and alkenals, which react with TBA to produce the pink chromophores with maximum absorbance at 455 nm and 532 nm.[89,90] Notably, no significant spectral changes were observed for the reaction between $Fe^{III}(ClO_4)_3{\cdot}6H_2O$ and linoleic acid treated with TBA over approximately 5 hours. In contrast, $[Fe^{III}(L^{5R})(OH)]^{1+}$ complexes displayed time-dependent changes. This observation underscores the notion that the mere presence of Fe^{3+} ions is inadequate to induce the peroxidation of fatty acids; instead, a well-structured Fe^{III}–OH species meeting the necessary thermodynamic criteria is essential for exhibiting lipoxygenase-like reactivity. In all kinetic runs, the growth of the 532 nm band was monitored, displaying good first-order behavior. Figure 6a shows a representative spectral growth and the corresponding kinetic time trace for the peroxidation of linoleic acid catalyzed by $\mathbf{4}^{OH}$ in the presence of TBA. The pseudo-first-order rate constant (k_{obs}) for each kinetic run was determined from the graphs shown in Figure S47. Plotting these pseudo-first-order rate constants (k_{obs}) against linoleic acid concentrations produced good linear fittings passing through the origin (Figure 6b). The slopes of these lines gave the second-order rate constant (k_2) values. The observed k_2 values demonstrated a substituent-dependent order: $[Fe^{III}(L^{5NO2})(OH)]^{1+}$ ($15.02 \times 10^{-3}\ M^{-1}s^{-1}$) > $[Fe^{III}(L^{5Cl})(OH)]^{1+}$ ($9.68 \times 10^{-3}\ M^{-1}s^{-1}$) > $[Fe^{III}(L^{5H})(OH)]^{1+}$ ($6.67 \times 10^{-3}\ M^{-1}s^{-1}$) > $[Fe^{III}(L^{5OMe})(OH)]^{1+}$ ($5.55 \times 10^{-3}\ M^{-1}s^{-1}$). This reactivity trend is consistent with the BDFE order (*vide supra*). However, the range of k_2 values in this series shows only a roughly 3-fold variation, which tallies with the narrow range observed in BDFE values.

Discussion on HAA reactions and possible pathways. Complexes $\mathbf{1}^{OH}$–$\mathbf{4}^{OH}$ catalyze the lipid peroxidation reactions through the initial generation of an allylic radical. To support this hypothesis, we investigated the peroxidation process of linoleic acid with complex $\mathbf{2}^{OH}$, introducing a stable free radical (2,2,6,6-tetramethylpiperidin-1-yl)oxyl (TEMPO•) under the previously mentioned conditions. As demonstrated in Figure S48, adding TEMPO• almost entirely suppressed the peroxidation of linoleic acid. This finding substantiates our claim of allylic radical formation. The TEMPO• radical captured the allylic radical, obstructing the further progression of the peroxidation reaction. In this reaction, the rate-determining step likely involves the H-atom abstraction from the allylic C–H bond by the Fe(III)-hydroxo complexes. Unfortunately, we could not verify this claim since di-deuterated linoleic acid was not readily accessible. Instead, we examined the hydrogen atom abstraction reactions for substrates 9H-xanthene and its deuterated analog with complex $\mathbf{2}^{OH}$ in CH_3OH and CD_3OD to evaluate the kinetic isotopic effect (KIE). The observed KIE value of 2.1 confirmed that the $\mathbf{2}^{OH}$ complex undergoes rate-determining hydrogen atom abstraction from C–H substrates. The ferric complexes are anticipated to reduce to ferrous states during HAA reactions. The conversion of ferric to ferrous was monitored using EPR spectroscopy during the reaction between complex $\mathbf{2}^{OH}$ and linoleic acid in methanol under inert conditions. Figure S49 illustrates that the reaction sample became EPR silent while treating the ferric complex with linoleic acid, indicating the conversion to the Fe(II) state. However, the EPR signal for the allylic radical species was not detected due to rapid quenching.

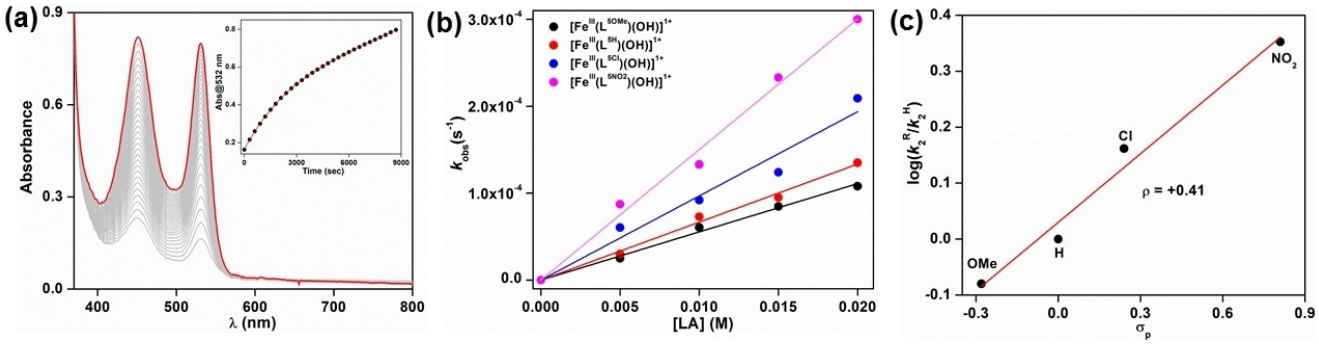

Figure 6. (a) Representative spectral changes and kinetic time-trace of the peroxidation process of linoleic acid (LA, 15 mM) in the presence of TBA (15 mM), catalyzed by $[Fe^{III}(L^{5NO2})(OH)]^{1+}$ ($\mathbf{4}^{OH}$) (0.25 mM) at 30 °C in a pH 7.15 water/methanol (48 : 52, v/v) medium. Plots of (b) pseudo-first-order rate constants (k_{obs}, s^{-1}) *vs* linoleic acid concentrations and (c) $\log(k_2^{(R)}/k_2^{(H)})$ *vs* the Hammett substituent constants (σ_p) for HAA reactivities with $[Fe^{III}(L^{5R})(OH)]^{1+}$ complexes (R = OMe, H, Cl and NO_2).

The allylic radical formation involves the transfer of a hydrogen atom ($H^{\bullet} = H^{+} + e^{-}$) from the allylic C–H bond to $[Fe^{III}(L^{5R})(OH)]^{1+}$. Figure 7 depicts three different pathways for proton-electron transfer: (i) ET-PT, (ii) PT-ET, and (iii) CPET. The redox potentials of $[Fe^{III}(L^{5R})(OH)]^{1+}/[Fe^{II}(L^{5R})(OH)]$ couples were experimentally determined to be 0.070 V, 0.101 V, 0.138 V, and 0.182 V *vs* NHE for R = OMe, H, Cl and NO_2, respectively (Table 2). The redox potential for allylic C(11)–H of linoleic acid was computed to be $E_{(C-H)\bullet+/(C-H)} = 1.69$ V *vs* NHE. Thus, the electron transfer (ET1) from the allylic C(11)–H of linoleic acid to $[Fe^{III}(L^{5R})(OH)]^{1+}$ is predicted to be non-spontaneous ($\triangle G_{ET1} \gg 0$). Similarly, the proton transfer (PT1) from the allylic C(11)–H (computed $pK_a^{(C-H)} = 39.54$) to $[Fe^{III}(L^{5R})(OH)]^{1+}$ is also expected to be non-spontaneous ($\triangle G_{PT1} \gg 0$). Consequently, the stepwise ET-PT or PT-ET should become energetically unfeasible due to the apparent highly endergonic initial ET1 or PT1 step. However, the concerted electron-proton transfer (CPET) may offer energetic advantages over individual electron and proton transfer. The calculated pK_a of the allylic C(11)-H cation radical ($(C-H)^{\bullet+}$) is −18.78, signifying the highly acidic nature of the $(C-H)^{\bullet+}$ bond. Therefore, PT2 from the linoleic acid C(11)–H cation radical to $[Fe^{II}(L^{5R})(OH)]$ will be highly exergonic ($\triangle G_{PT2} \ll 0$). In another scenario, ET2 from the allylic carbanion (computed $E_{(C\bullet/C-)} = -1.78$ V *vs* NHE) to $[Fe^{III}(L^{5R})(OH_2)]^{2+}$ will also be highly exergonic ($\triangle G_{ET2} \ll 0$). Thus, the CPET would be energetically favorable, as the follow-up PT2 and ET2 steps are highly spontaneous. So, in the present case, the thermodynamic argument precludes initial electron or proton transfer, providing strong evidence for a concerted process. Following Hess's law, the driving force for the hydrogen atom transfer can be expressed as $\triangle G_H = \triangle G_{ET1} + \triangle G_{PT2} = \triangle G_{PT1} + \triangle G_{ET2} < 0$ (Table S4).

The CPET may occur either synchronously or asynchronously. Synchronous proton-electron transfer happens when $\Delta G_{ET1} = \Delta G_{PT2}$ or $\Delta G_{PT1} = \Delta G_{ET2}$. In such cases, it suggests that the electronic effects of substituents on reaction rates are negligible, as the electronic influences on ET and PT cancel out each other (*i.e.* $\Delta\Delta G_{ET1} = -\Delta\Delta G_{PT2}$ or $\Delta\Delta G_{PT1} = -\Delta\Delta G_{ET2}$).[44] Consequently, the Hammett slope (ρ) would be nearly zero for an ideal synchronous CPET reaction. However, for the present $[Fe^{III}(L^{5R})(OH)]^{1+}$ complexes, HAA rates vary with the 5-R group of the L^{5R} ligands. The plot of $\log(k_2^{(R)}/k_2^{(H)})$ *vs* the Hammett substituent constants (σ_{para}) exhibits a good linear correlation ($R^2 = 0.97$) with a slope of $\rho = +0.41 \pm 0.04$ (Figure 6c), indicating that the HAA reaction is responsive to the electronic effects of the 5-R substituents of the L^{5R} ligands.

The ET reactions from decamethylferrocene ($Me_{10}Fc$; $E_{1/2} = 0.14$ V *vs* NHE) to $[Fe^{III}(L^{5R})(OH)]^{1+}$ were studied in a pH 7.15 aqueous pipes buffer/MeOH solvent mixture (96 : 4, v/v) at 303 K under anaerobic conditions. These studies evaluated the electronic influences of the 5-R groups on ET rates. The kinetics of ET reactions were monitored by tracking the increase in absorbance at the 780 nm band ascribed to $Me_{10}Fc^{+}$ over time using a UV-vis spectrophotometer. All ET reactions exhibited first-order kinetics. Figure S50 shows the representative spectral changes and the kinetic time trace for ET from $Me_{10}Fc$ to the

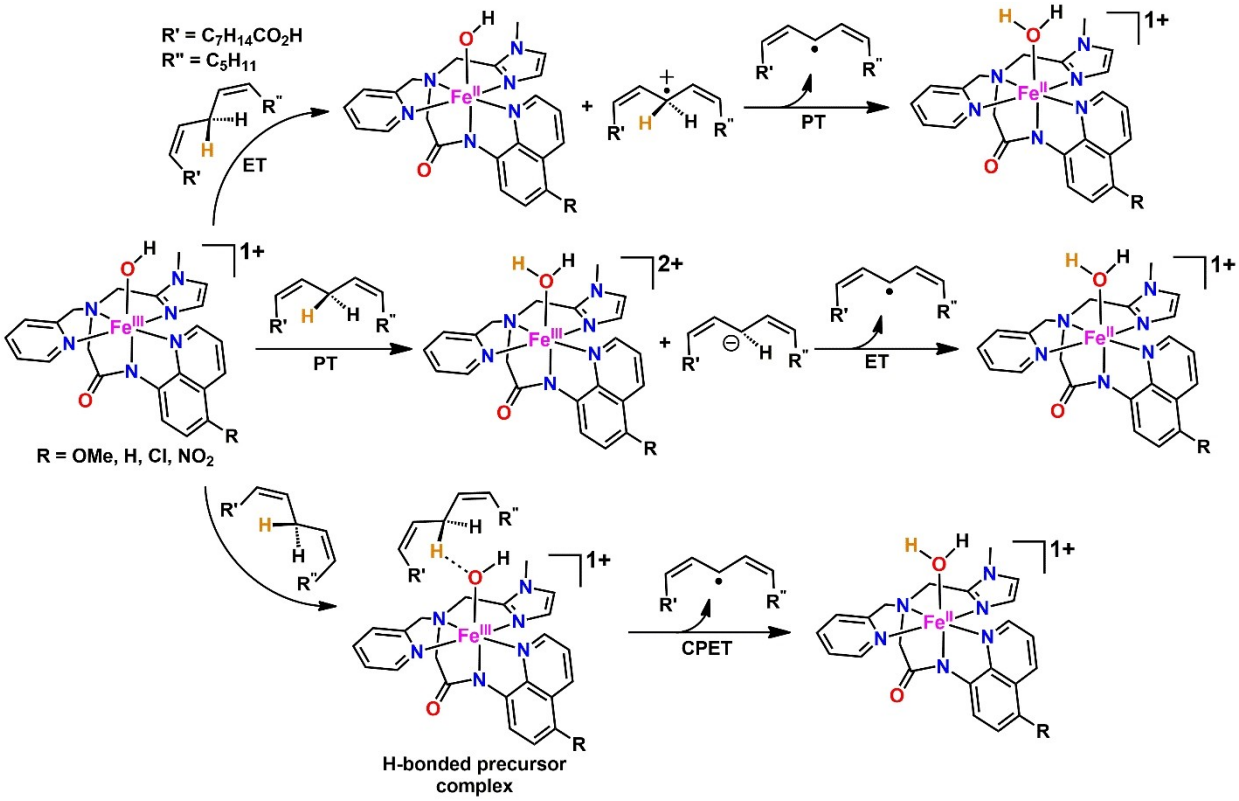

Figure 7. Plausible electron-proton transfer pathways for HAA from linoleic acid C(11) –H bond to $[Fe^{III}(L^{5R})(OH)]^{1+}$ (R = OMe, H, Cl and NO_2).

$[Fe^{III}(L^{5H})(OH)]^{1+}$ complex. The second-order electron transfer rates (k_{et}) were determined from the slopes of the plots of pseudo-first-order rate constants (k_{et}^{obs}) *vs* [$Me_{10}Fc$], as depicted in Figure S51. The Hammett plot of $\log(k_{et}^{(R)}/k_{et}^{(H)})$ *vs* σ_p demonstrates a reasonably linear correlation ($R^2 = 0.96$) with a slope of $\rho = +0.86 \pm 0.10$ (Figure S52). Notably, the ρ value for ET from $Me_{10}Fc$ to $[Fe^{III}(L^{5R})(OH)]^{1+}$ is much larger than the ρ value (+0.41) for HAA reactions, indicating that a pure ET is more sensitive to substituents' electronic effects. For the present HAA reactions, the observed decrease in the ρ value suggests that the electronic influences of substituents on changing redox potentials are partially offset by concurrent changes in pK_a values in the opposite direction. This lowering of the ρ value thus accounts for the simultaneous occurrence of electron and proton transfers in the rate-determining step. However, the positive ρ value suggests emerging an electron-deficient catalyst surface in the transition state with more ET character than PT. In such cases, HAA occurs *via* an oxidative asynchronous CPET pathway, as reported in the literature for the HAA from 4-MeO-2,6-$^tBu_2C_6H_2OH$ to $[(dpaq^{5R})Mn^{III}(OH)]^{1+}$ (R = OMe, Me, H, Cl, NO_2).[44] On the contrary, Borovik *et al.* found a negative Hammett correlation for the hydrogen atom transfer reaction from 9,10-dihydroanthracene (DHA) to $[Mn^{III}H_3bpuea\text{-}R(O)]^{2-}$ (R = OMe, H, F, Cl, CF_3). In that case, a mechanistic scenario favoring an asynchronous transition state dominated by PT was suggested.[91]

Srnec *et al.* introduced a thermodynamic factor, η, to quantify the degree of asynchronicity in proton-electron transfers during concerted HAA reactions.[54] A positive η value specifies an oxidative asynchronous CPET, while a negative η represents a basic asynchronous CPET process. In the case of synchronous CPET, η tends to zero. We determined the η values for HAA reactions between $[Fe^{III}(L^{5R})(OH)]^{1+}$ complexes and the substrate linoleic acid using Srnec's method outlined in the Supporting Information. Interestingly, we found positive η values for all Fe^{III}-hydroxo complexes, ranging from 276 mV to 365 mV (Table 3), which further supports oxidative asynchronous CPET for all HAA reactions. The logarithm of k_2 shows a good linear correlation with the asynchronicity factors η ($R^2 = 0.98$), indicating that reactivity increases proportionally with asynchronicity, as depicted in Figure S53. This finding aligns with Srnec's proposition that increased asynchronicity lowers the energy barrier, resulting in greater reactivity.

Furthermore, the activation parameters for hydrogen atom transfer from linoleic acid to $[Fe^{III}(L^{5R})(OH)]^{1+}$ were determined from the Eyring plots, as shown in Figure 8. Table 3 presents the data for activation enthalpies ($\Delta H^{\neq}$) and entropies ($\Delta S^{\neq}$). For all complexes, the $\Delta H^{\neq}$ values are nearly the same within the experimental error. Similarly, the $\Delta S^{\neq}$ values align closely with one another. This consistency implies that all complexes adhere to a similar reaction pathway, irrespective of the 5-R substituents. The large negative $\Delta S^{\neq}$ values indicate a bimolecular transition state, where two reactants must come together for the reaction to proceed. Such an ordered transition state is consistent with the CPET path reported in the literature.[36,44]

Table 3. Asynchronicity factors (η) and thermodynamic parameters for hydrogen atom transfer reactions from linoleic acid C(11)–H bond to $[Fe^{III}(L^{5R})(OH)]^{1+}$ (R = OMe, H, Cl, NO_2).

R	η (mV)	$\Delta H^{\neq}$ (kcal mol^{-1})	$\Delta S^{\neq}$ (cal mol^{-1} K^{-1})
OMe	276	11.86	−38.34
H	301	11.75	−38.20
Cl	332	11.68	−37.80
NO_2	365	11.56	−37.38

HAA reactivity of Fe(III)–OH_2 complexes. The HAA reactivity of $[Fe^{III}(L^{5R})(OH_2)]^{2+}$ complexes towards the linoleic acid substrate was examined under similar conditions that were used for the $[Fe^{III}(L^{5R})(OH)]^{1+}$ complexes. The experiments were carried out at a pH of 3.5 to ensure the presence of the "Fe(III)–OH_2" complexes in solution, as indicated by Pourbaix diagrams. All $[Fe^{III}(L^{5R})(OH_2)]^{2+}$ complexes demonstrated effective catalysis of the HAA reactions. Proton transfer in these reactions might have occurred to the ligand instead of the coordinated water since ligand L^{5R} contains multiple potential proton acceptor sites, such as pyridine, imidazole, and anionic amide groups. A thermodynamic cycle, taking into account the redox potentials of $[Fe^{III}(L^{5R})(OH_2)]^{2+}/[Fe^{II}(L^{5R})(OH_2)]^{1+}$ couples and the pK_a values of $[Fe^{II}(\mathbf{H}L^{5R})(OH_2)]^{2+}$ in an aqueous medium, was employed to determine the BDFEs of H-L^{5R} bonds in the product $[Fe^{II}(H\text{-}L^{5R})(OH_2)]^{2+}$ (Scheme 4). The estimated BDFEs(H-L^{5R}) for $[Fe^{II}(H\text{-}L^{5OMe})(OH_2)]^{2+}$, $[Fe^{II}(H\text{-}L^{5H})(OH_2)]^{2+}$, $[Fe^{II}(H\text{-}L^{5Cl})(OH_2)]^{2+}$, and $[Fe^{II}(H\text{-}L^{5NO2})(OH_2)]^{2+}$ are 65.70 kcal/mol, 65.98 kcal/mol, 66.54 kcal/mol, and 66.92 kcal/mol, respectively. These BDFEs(H-L^{5R}) closely match the bond strength of the allylic C(11)–H bond in linoleic acid, enabling $[Fe^{III}(L^{5R})(OH_2)]^{2+}$ complexes to abstract hydrogen from linoleic acid. The evaluations showed that the BDFEs(H-L^{5R}) remained almost consistent despite changing the 5-R group from electron-donating to electron-withdrawing.

Akin to the Fe(III)-hydroxo complexes, the second-order rates of hydrogen transfer reactions from linoleic acid to $[Fe^{III}(L^{5R})(OH_2)]^{2+}$ complexes followed a substituent dependent order: $[Fe^{III}(L^{5NO2})(OH_2)]^{2+}$ (92.13×10^{-3} M^{-1} s^{-1}) > [Fe^{III}-

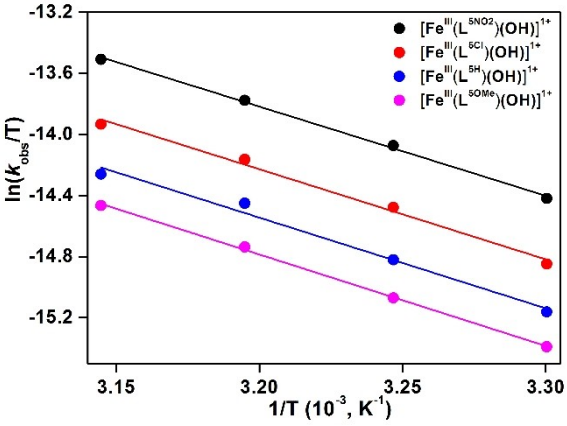

Figure 8. Eyring plots for HAA reactions from linoleic acid to $[Fe^{III}(L^{5R})(OH)]^{1+}$ in pH 7.15 water/methanol (48:52, v/v) at the temperature range of 303–318 K.

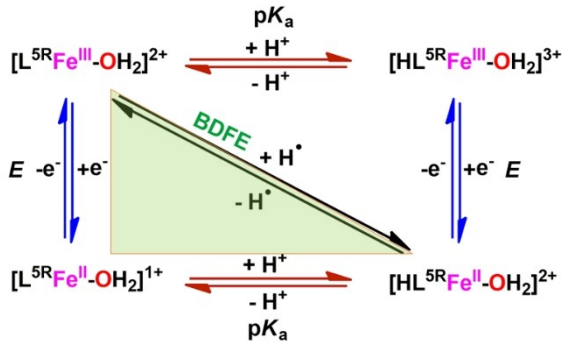

Scheme 4. Thermodynamic square scheme for determining the BDFEs of H–L^{5R} bonds in $[HL^{5R}Fe^{II}\text{-}OH_2]^{2+}$.

$(L^{5Cl})(OH_2)]^{2+}$ ($51.64 \times 10^{-3}\ M^{-1}\,s^{-1}$) > $[Fe^{III}(L^{5H})(OH_2)]^{2+}$ ($35.13 \times 10^{-3}\ M^{-1}\,s^{-1}$) > $[Fe^{III}(L^{5OMe})(OH_2)]^{2+}$ ($25.18 \times 10^{-3}\ M^{-1}\,s^{-1}$) (Figure 9a). Remarkably, $[Fe^{III}(L^{5R})(OH_2)]^{2+}$ complexes showed ~5 times faster HAA reactions compared to their corresponding $[Fe^{III}(L^{5R})(OH)]^{1+}$ complexes. Fukuzumi and Nam *et al.* also observed significantly higher HAA reactivity with Mn^{III}-aqua complexes, $[(dpaq^{5R})Mn^{III}(OH_2)]^{2+}$, compared to the corresponding Mn^{III}-hydroxo complexes, $[(dpaq^{5R})Mn^{III}(OH)]^{1+}$.[44,45] The Hammett plot of hydrogen atom transfer from linoleic acid to $[Fe^{III}(L^{5R})(OH_2)]^{2+}$ complexes displays a good linear correlation ($R^2 = 0.98$) with a slope of $\rho = +0.52 \pm 0.03$ (Figure 9b), higher than the ρ value (+0.41) obtained for $[Fe^{III}(L^{5R})(OH)]^{1+}$ complexes. The positive ρ value indicates that HAA occurs *via* the oxidative asynchronous CPET pathway for the $[Fe^{III}(L^{5R})(OH_2)]^{2+}$ complexes as well. The negative entropy of activation ($\Delta S^{\neq}$) is consistent with a bimolecular transition state required for the CPET pathway (Figure S54, Table S5).[44] However, the transition state in aqua complexes may have a more dominant ET character than hydroxo complexes. This proposition may be realized by considering the higher potential for the "Fe^{III}–OH_2"/"Fe^{II}–OH_2" couple in comparison to the "Fe^{III}–OH"/"Fe^{II}–OH" couple. The increased ET character in the transition state could reduce the energy barrier, which accounts for the faster rate observed for Fe(III)-aqua complexes relative to Fe(III)-hydroxo complexes.

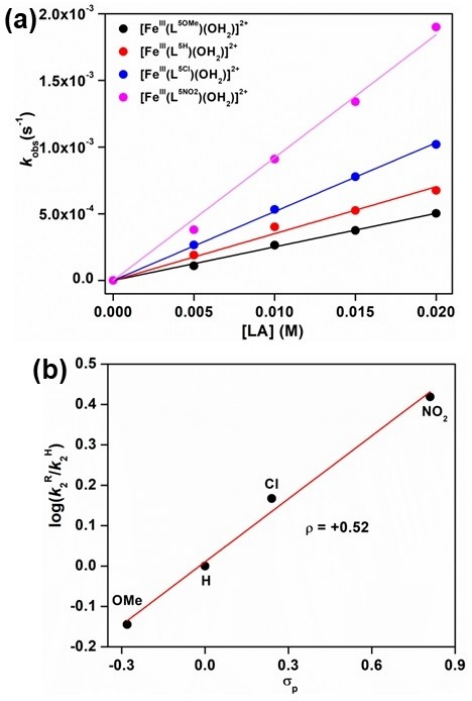

Figure 9. Plots of (a) pseudo-first-order rate constants (k_{obs}, s^{-1}) *vs* linoleic acid (LA) concentrations and (b) $\log(k_2^{(R)}/k_2^{(H)})$ *vs* the Hammett substituent constants (σ_p) for hydrogen atom transfer from linoleic acid C(11)–H bond to $[Fe^{III}(L^{5R})(OH_2)]^{2+}$ (R = OMe, H, Cl and NO_2) in a pH 3.5 water/methanol (48:52, v/v) medium at 30 °C.

Summary and Conclusions

A series of mononuclear Fe^{III}-aqua complexes, $[Fe^{III}(L^{5R})(OH_2)]^{2+}$ ($\mathbf{1^{H2O}}$–$\mathbf{4^{H2O}}$), were prepared by varying the substituents at the 5-position of the quinoline moiety of the L^{5R} ligand with electron-donating and -withdrawing groups (R = OMe, H, Cl, NO_2). These complexes were characterized using spectroscopic and analytical methods. The Fe^{III}-hydroxo complexes, $[Fe^{III}(L^{5R})(OH)]^{1+}$ ($\mathbf{1^{OH}}$–$\mathbf{4^{OH}}$), were generated *in situ* from their corresponding aqua complexes in an aqueous medium at pH ~7. Alternatively, treating the ferric aqua complexes with one equivalent of a base in methanol produced the Fe(III)-hydroxo complexes. All $[Fe^{III}(L^{5R})(OH)]^{1+}$ complexes exhibited lipoxygenase-like reactivity, effectively catalyzing the linoleic acid peroxidation under aerobic conditions. The reaction occurred through an initial hydrogen atom transfer from linoleic acid C(11)–H bond to $[Fe^{III}(L^{5R})(OH)]^{1+}$ in a rate-determining step. The electronic effects of the 5-R groups influence the reaction rates, which increase as the electron-withdrawing character of the substituent increases. The BDFE analysis of the Fe^{II}(HO–H) bond in the product $[Fe^{II}(L^{5R})(HO\text{–}H)]^{1+}$ revealed that the redox potential increase was insufficiently compensated by the pK_a decrease, giving an overall rise in BDFEs with changing 5-R groups from electron-donating to -withdrawing. The Hammett plot of $\log(k_2^{(R)}/k_2^{(H)})$ *vs* σ_p shows a linear correlation with a slope of $\rho = +0.41$. This ρ value is significantly lower than the slope (0.86) obtained for outer-sphere ET from $Me_{10}Fc$ to $[Fe^{III}(L^{5R})(OH)]^{1+}$. Also, the asynchronicity factor (η) was positive for all these HAA reactions. Based on these observations, an oxidative asynchronous CPET was proposed for the HAA reaction from linoleic acid to $[Fe^{III}(L^{5R})(OH)]^{1+}$. The large negative $\triangle S^{\neq}$ values indicate a bimolecular ordered transition state consistent with the CPET mechanism. The HAA reactivity with aqua complexes $[Fe^{III}(L^{5R})(OH_2)]^{2+}$ also revealed a similar oxidative asynchronous CPET mechanism. However, a higher ρ value (+0.52) was observed for the aqua complexes, suggesting a greater dominance of the ET character in the transition state compared to the hydroxo complexes. This higher asynchronicity in CPET can potentially lower the energy barrier, resulting in a higher reaction rate for aqua complexes to their hydroxo analogs. Thus, this study provides valuable insights into the asynchronous CPET mechanism, indicating that a higher imbalance in

ET-PT contributions may be advantageous in hydrogen atom abstraction reactions.

Keywords: Iron complex · Hydrogen atom abstraction · C–H bond activation · Asynchronous CPET · Linoleic acid · Kinetics

Supporting Information Summary

This segment includes the experimental section, synthetic procedures, characterization data, instrumentation, structure determination, kinetic measurements, computational details, figures, tables, and coordinates of the optimized structures.

Deposition Number 2336880 (for $\mathbf{3^{H2O}(ClO_4)_2}$) contains the supplementary crystallographic data for this paper. These data are provided free of charge by the joint Cambridge Crystallographic Data Center and Fachinformationszentrum Karlsruhe Access Structures service.

Author Contributions

MM performed compound synthesis, characterizations, experimental work, and data analysis. He also prepared the initial draft of the manuscript. AS carried out DFT calculations. SKB participated in valuable discussions. SM supervised the project, arranged funding, and wrote the manuscript.

Acknowledgments

This work was funded by the Science and Engineering Research Board (SERB), Government of India (Project No. EMR/2015/001136 to SM). SM acknowledges the financial support from the Council of Scientific and Industrial Research [Project No. 01(3052)/21/EMR-II], Government of India. MM gratefully acknowledges IIT Kharagpur for the PhD fellowship. SM and MM thank the Central Research Facility (CRF) and the Department of Chemistry, IIT Kharagpur, for the instrumental facilities (EPR, NMR, ATR-IR, ESI-MS, and X-ray). SM thanks the DST-FIST program (SR/FST/CSII-026/2013) for providing the NMR facility to the Department of Chemistry and appreciates the PARAM SHAKTI computing resources at IIT Kharagpur. SM acknowledges the Central Library at IIT Kharagpur for providing the funds for open access. All authors appreciate the reviewer's invaluable feedback during the revision stage.

Conflict of Interests

There are no conflicts to declare.

Data Availability Statement

The data that support the findings of this study are available in the supplementary material of this article.

[1] B. A. Arndtsen, R. G. Bergman, T. A. Mobley, T. H. Peterson, *Acc. Chem. Res.* **1995**, *28*, 154–162.
[2] S. K. Sinha, S. Guin, S. Maiti, J. P. Biswas, S. Porey, D. Maiti, *Chem. Rev.* **2022**, *122*, 5682–5841.
[3] M. Inoue, H. Tsurugi, K. Mashima, *Coord. Chem. Rev.* **2022**, *473*, 214810.
[4] J. H. Docherty, T. M. Lister, G. Mcarthur, M. T. Findlay, P. Domingo-Legarda, J. Kenyon, S. Choudhary, I. Larrosa, *Chem. Rev.* **2023**, *123*, 7692–7760.
[5] L. Que Jr, W. B. Tolman, *Nature* **2008**, *455*, 333–340.
[6] V. A. Larson, B. Battistella, K. Ray, N. Lehnert, W. Nam, *Nat. Rev. Chem.* **2020**, *4*, 404–419.
[7] A. B. McQuarters, M. W. Wolf, A. P. Hunt, N. Lehnert, *Angew. Chem. Int. Ed.* **2014**, *53*, 4750–4752.
[8] J. L. Grant, M. E. Mitchell, T. M. Makris, *Proc. Natl. Acad. Sci. U. S. A.* **2016**, *113*, 10049–10054.
[9] J. L. Lee, D. L. Ross, S. K. Barman, J. W. Ziller, A. S. Borovik, *Inorg. Chem.* **2021**, *60*, 13759–13783.
[10] A. S. Borovik, *Chem. Soc. Rev.* **2011**, *40*, 1870–1874.
[11] J. J. D. Sacramento, D. P. Goldberg, *Acc. Chem. Res.* **2018**, *51*, 2641–2652.
[12] S. Kal, S. Xu, L. Que Jr, *Angew. Chem. Int. Ed.* **2020**, *59*, 7332–7349.
[13] W. Nam, Y.-M. Lee, S. Fukuzumi, *Acc. Chem. Res.* **2014**, *47*, 1146–1154.
[14] S. Kal, L. Que, *J. Biol. Inorg. Chem.* **2017**, *22*, 339–365.
[15] M. Srnec, E. I. Solomon, *J. Am. Chem. Soc.* **2017**, *139*, 2396–2407.
[16] L. C. Blasiak, F. H. Vaillancourt, C. T. Walsh, C. L. Drennan, *Nature* **2006**, *440*, 368–371.
[17] X. Huang, J. T. Groves, *Chem. Rev.* **2018**, *118*, 2491–2553.
[18] D. Usharani, D. C. Lacy, A. S. Borovik, S. Shaik, *J. Am. Chem. Soc.* **2013**, *135*, 17090–17104.
[19] T. J. Collins, A. D. Ryabov, *Chem. Rev.* **2017**, *117*, 9140–9162.
[20] A. H. Follmer, A. S. Borovik, *Dalton Trans.* **2023**, *52*, 11005–11016.
[21] D. B. Rice, A. A. Massie, T. A. Jackson, *Acc. Chem. Res.* **2017**, *50*, 2706–2717.
[22] T. H. Parsell, M.-Y. Yang, A. S. Borovik, *J. Am. Chem. Soc.* **2009**, *131*, 2762–2763.
[23] X. Wu, M. S. Seo, K. M. Davis, Y.-M. Lee, J. Chen, K.-B. Cho, Y. N. Pushkar, W. Nam, *J. Am. Chem. Soc.* **2011**, *133*, 20088–20091.
[24] R. A. Baglia, K. A. Prokop-Prigge, H. M. Neu, M. A. Siegler, D. P. Goldberg, *J. Am. Chem. Soc.* **2015**, *137*, 10874–10877.
[25] H. Kotani, S. Kaida, T. Ishizuka, K. Mieda, M. Sakaguchi, T. Ogura, Y. Shiota, K. Yoshizawa, T. Kojima, *Inorg. Chem.* **2018**, *57*, 13929–13936.
[26] N. Zhao, M. K. Goetz, J. E. Schneider, J. S. Anderson, *J. Am. Chem. Soc.* **2023**, *145*, 5664–5673.
[27] H. Kotani, H. Shimomura, K. Ikeda, T. Ishizuka, Y. Shiota, K. Yoshizawa, T. Kojima, *J. Am. Chem. Soc.* **2020**,*142*,16982–16989.
[28] G. Yin, A. M. Danby, D. Kitko, J. D. Carter, W. M. Scheper, D. H. Busch, *J. Am. Chem. Soc.* **2007**, *129*, 1512–1513.
[29] J. P. T. Zaragoza, M. A. Siegler, D. P. Goldberg, *J. Am. Chem. Soc.* **2018**, *140*, 4380–4390.
[30] Y. Lee, G. L. Tripodi, D. Jeong, S. Lee, J. Roithova, J. Cho, *J. Am. Chem. Soc.* **2022**, *144*, 20752–20762.
[31] K. Keshari, M. Bera, L. Velasco, S. Munshi, G. Gupta, D. Moonshiram, S. Paria, *Chem. Sci.* **2021**, *12*, 4418–4424.
[32] C. R. Goldsmith, T. D. P. Stack, *Inorg. Chem.* **2006**, *45*, 6048–6055.
[33] C. R. Goldsmith, A. P. Cole, T. D. P. Stack, *J. Am. Chem. Soc.* **2005**, *127*, 9904–9912.
[34] H. Gao, J. T. Groves, *J. Am. Chem. Soc.* **2017**, *139*, 3938–3941.
[35] E. Dobbelaar, C. Rauber, T. Bonck, H. Kelm, M. Schmitz, M. E. de Waal Malefijt, J. E. M. N. Klein, H.-J. Kruger, *J. Am. Chem. Soc.* **2021**, *143*, 13145–13155.
[36] G. B. Wijeratne, B. Corzine, V. W. Day, T. A. Jackson, *Inorg. Chem.* **2014**, *53*, 7622–7634.
[37] M. K. Coggins, L. M. Brines, J. A. Kovacs, *Inorg. Chem.* **2013**, *52*, 12383–12393.
[38] W.-M. Ching, A. Zhou, J. E. M. N. Klein, R. Fan, G. Knizia, C. J. Cramer, Y. Guo, L. Que Jr, *Inorg. Chem.* **2017**, *56*, 11129–11140.
[39] D. Dhar, W. B. Tolman, *J. Am. Chem. Soc.* **2015**, *137*, 1322–1329.
[40] D. Dhar, G. M. Yee, T. F. Markle, J. M. Mayer, W. B. Tolman, *Chem. Sci.* **2017**, *8*, 1075–1085.
[41] C. R. Goldsmith, R. T. Jonas, T. D. P. Stack, *J. Am. Chem. Soc.* **2002**, *124*, 83–96.

[42] F. Mei, C. Ou, G. Wu, L. Cao, F. Han, X. Meng, J. Li, D. Li, Z. Liao, *Dalton Trans.* **2010**, *39*, 4267–4269.
[43] G. B. Wijeratne, V. W. Day, T. A. Jackson, *Dalton Trans.* **2015**, *44*, 3295–3306.
[44] J. Zhang, Y.-M. Lee, M. S. Seo, Y. Kim, E. Lee, S. Fukuzumi, W. Nam, *Inorg. Chem. Front.* **2022**, *9*, 3233–3243.
[45] M. Sankaralingam, Y.-M. Lee, D. G. Karmalkar, W. Nam, S. Fukuzumi, *J. Am. Chem. Soc.* **2018**, *140*, 12695–12699.
[46] W. Minor, J. Steczko, B. Stec, Z. Otwinowski, J. T. Bolin, R. Walter, B. Axelrod, *Biochemistry* **1996**, *35*, 10687–10701.
[47] J. C. Boyington, B. J. Gaffney, L. M. Amzel, *Science* **1993**, *260*, 1482–1486.
[48] S. A. Gillmor, A. Villasenor, R. Fletterick, E. Sigal, M. F. Browner, *Nat. Struct. Biol.* **1997**, *4*, 1003–1009.
[49] M. H. Glickman, J. P. Klinman, *Biochemistry* **1995**, *34*, 14077–14092.
[50] E. N. Segraves, T. R. Holman, *Biochemistry* **2003**, *42*, 5236–5243.
[51] C. Su, M. Sahlin, E. H. Oliw, *J. Biol. Chem.* **2000**, *275*, 18830–18835.
[52] A. Kostenko, K. Ray, A. T. Iavarone, A. R. Offenbacher, *Biochemistry* **2019**, *58*, 3193–3203.
[53] R. Tyburski, T. Liu, S. D. Glover, L. Hammarstrom, *J. Am. Chem. Soc.* **2021**, *143*, 560–576.
[54] D. Bím, M. Maldonado-Domíngueza, L. Rulíšek, M. Srnec, *Proc. Natl. Acad. Sci. U. S. A* **2018**, *115*, E10287–E10294.
[55] J. W. Darcy, S. S. Kolmar, J. M. Mayer, *J. Am. Chem. Soc.* **2019**, *141*, 10777–10787.
[56] M. Mandal, C. E. Elwell, C. J. Bouchey, W. B. Tolman, C. J. Cramer, *J. Am. Chem. Soc.* **2019**, *141*, 17236–17244.
[57] Y. Hitomi, K. Arakawa, T. Funabiki, M. Kodera, *Angew. Chem. Int. Ed.* **2012**, *51*, 3448–3452.
[58] Y. Hitomi, K. Arakawa, M. Kodera, *Chem. Eur. J.* **2013**, *19*, 14697–14701.
[59] S. Mandal, J. Mukherjee, F. Lloret, R. Mukherjee, *Inorg. Chem.* **2012**, *51*, 13148–13161.
[60] N. Podder, S. Dey, A. Anoop, S. Mandal, *Dalton Trans.* **2022**, *51*, 4338–4353.
[61] A. Kundu, S. Khan, S. Dey, C. Dutta, A. Anoop, S. Mandal, *Eur. J. Inorg. Chem.* **2019**, *2019*(2), 164–177.
[62] M. Nihei, T. Shiga, Y. Maeda, H. Oshio, *Coord. Chem. Rev.* **2007**, *251*, 2606–2621.
[63] H. H. Wickman, M. P. Klein, D. A. Shirley, *J. Chem. Phys.* **1965**, *42*, 2113–2117.
[64] R. Aasa, *J. Chem. Phys.* **1970**, *52*, 3919–3930.
[65] N. E. Domracheva, A. V. Pyataev, V. E. Vorobeva, E. M. Zueva, *J. Phys. Chem. B* **2013**, *117*, 7833–7842.
[66] V. E. Vorobeva, N. E. Domracheva, A. V. Pyataev, M. S. Gruzdev, U. V. Chervonova, *Low Temp. Phys.* **2015**, *41*, 15–19.
[67] S. Stoll, A. Schweiger, *J. Magn. Reson.* **2006**, *178*, 42–55.
[68] S. Stoll, R. D. Britt, *Phys. Chem. Chem. Phys.* **2009**, *11*, 6614–6625.
[69] S. Sundaresan, I. A. Kühne, C. T. Kelly, A. Barker, D. Salley, H. Müller-Bunz, A. K. Powell, G. G. Morgan, *Crystals* **2019**, *9*, 19.
[70] M. S. Gruzdev, V. E. Vorobeva, E. M. Zueva, U. V. Chervonova, M. M. Petrova, N. E. Domracheva, *Polyhedron* **2018**, *155*, 415–424.
[71] B. Dey, J. Cirera, S. Mehta, L. P. Ferreira, R. Arumugam, A. Mondal, P. N. Martinho, V. Chandrasekhar, *Cryst. Growth Des.* **2023**, *23*, 6668–6678.
[72] N. Domracheva, A. Pyataev, R. Manapov, M. Gruzdev, U. Chervonova, A. Kolker, *Eur. J. Inorg. Chem.* **2011**, 1219–1229.
[73] M. S. Shongwe, B. A. Al-Rashdi, H. Adams, M. J. Morris, M. Mikuriya, G. R. Hearne, *Inorg. Chem.* **2007**, *46*, 9558–9568.
[74] F. Li, K. K. Meier, M. A. Cranswick, M. Chakrabarti, K. M. V. Heuvelen, E. Munck, L. Que Jr, *J. Am. Chem. Soc.* **2011**, *133*, 7256–7259.
[75] K. Ramesh, R. Mukherjee, *J. Chem. Soc. Dalton Trans.* **1992**, 83–89.
[76] T. A. Corry, P. J. O'Malley, *J. Am. Chem. Soc.* **2020**, *142*, 10240–10243.
[77] M. S. Shongwe, C. H. Kaschula, M. S. Adsetts, E. W. Ainscough, A. M. Brodie, M. J. Morris, *Inorg. Chem.* **2005**, *44*, 3070–3079.
[78] P. Masarova, P. Zoufaly, J. Moncol, I. Nemec, J. Pavlik, M. Gembicky, Z. Travnicek, R. Boca, I. Salitros, *New. J. Chem.* **2015**, *39*, 508–519.
[79] F. Bou-Abdallah, N. D. Chasteen, *J. Biol. Inorg. Chem.* **2008**, *13*, 15–24.
[80] R. G. Wollmann, D. N. Hendrickson, *Inorg. Chem.* **1978**, *17*, 926–930.
[81] G. Musie, C.-H. Lai, J. H. Reibenspies, L. W. Sumner, M. Y. Darensbourg, *Inorg. Chem.* **1998**, *37*, 4086–4093.
[82] R. M. Davydov, J. Smieja, S. A. Dikanov, Y. Zang, L. Que Jr, M. K. Bowman, *JBIC* **1999**, *49*, 292–301.
[83] S. Ogo, R. Yamahara, M. Roach, T. Suenobu, M. Aki, T. Ogura, T. Kitagawa, H. Masuda, S. Fukuzumi, Y. Watanabe, *Inorg. Chem.* **2002**, *41*, 5513–5520.
[84] H. S. Soo, A. C. Komor, A. T. Iavarone, C. J. Chang, *Inorg. Chem.* **2009**, *48*, 10024–10035.
[85] D. B. Rice, A. Munasinghe, E. N. Grotemeyer, A. D. Burr, V. W. Day, T. A. Jackson, *Inorg. Chem.* **2019**, *58*, 622–636.
[86] F. G. Bordwell, J.-P. Cheng, G.-Z. Ji, A. V. Satish, X. Zhang, *J. Am. Chem. Soc.* **1991**, *113*, 9790–9795.
[87] R. G. Agarwal, S. C. Coste, B. D. Groff, A. M. Heuer, H. Noh, G. A. Parada, C. F. Wise, E. M. Nichols, J. J. Warren, J. M. Mayer, *Chem. Rev.* **2022**, *122*, 1–49.
[88] L. M. Brines, M. K. Coggins, P. C. Y. Poon, S. Toledo, W. Kaminsky, M. L. Kirk, J. A. Kovacs, *J. Am. Chem. Soc.* **2015**, *137*, 2253–2264.
[89] V. Nair, G. A. Turner, *Lipids* **1984**, *19*, 804–805.
[90] A. de las Heras, A. Schoch, M. Gibis, A. Fischer, *Eur. Food Res. Technol.* **2003**, *217*, 180–184.
[91] S. K. Barman, J. R. Jones, C. Sun, E. A. Hill, J. W. Ziller, A. S. Borovik, *J. Am. Chem. Soc.* **2019**, *141*, 11142–11150.

Manuscript received: March 22, 2024
Accepted manuscript online: July 2, 2024
Version of record online: August 20, 2024